AIAA JOURNAL
Vol. 48, No. 2, February 2010

Automatic Balancing of Bladed-Disk/Shaft System via Passive Autobalancer Devices

H. A. DeSmidt*
University of Tennessee, Knoxville, Tennessee 37996-2210

DOI: 10.2514/1.43832

Autobalancers for rotor/bearing systems are passive devices consisting of eccentrically mounted balance masses that freely revolve around the rotor's axis of rotation. At certain supercritical speeds, the balancer mass positions naturally adjust to cancel the rotor imbalance. This automatic-balancing phenomena occurs as a result of nonlinear dynamic interaction between the balancer masses and the rotor's lateral vibration. Previous studies have found that autobalancers can effectively compensate for mass imbalance in planar rigid rotors such as hard-disk drives and flywheels, however, their use in bladed-disk and turbomachinery applications has not been previously considered. This study explores the dynamics and stability of a flexible bladed-disk/rotor-bearing system equipped with a dual-ball automatic-balancing device. It is found that the autobalancer effectively compensates for both mass and aerodynamic imbalances produced by a bladed-loss condition over a wide revolutions/minute range at speeds above the first lateral natural frequency. It is also shown that for stable automatic balancing to occur, the ratio of automatic balancer damping to the blade aerodynamic drag coefficient must be above some critical value. The analysis demonstrates that the automatic balancer is able to simultaneously reduce both bearing loads and blade deflections for a simulated blade-loss event.

Nomenclature

A	=	linearized system matrix
$\{\mathbf{a}_i\}$	=	blade-fixed coordinate frame, $[\mathbf{a}_{1i}, \mathbf{a}_{2i}, \mathbf{a}_{3i}]$
b_i	=	blade chord, m
$\mathbf{C}$, $\mathbf{C}_{\text{blisk}}$, $\mathbf{C}_{\text{AB}}$, $\mathbf{C}_{\text{aero}}$	=	damping matrices
C_d	=	blade drag coefficient (nondimensional)
c_b	=	ball/track viscous damping, kg/s
c_d	=	blade drag coefficient per unit length, kg/m^2
c_s	=	bearing-support damping, kg/s
c_t	=	shaft torsional damping, N-m-s
c_1, c_2, c_3, c_4	=	equilibrium polynomial coefficients
D	=	Rayleigh dissipation function, N-m
D_b	=	ball diameter, m
E	=	blade elastic modulus, N/m^2
e_{cc}	=	hub eccentricity, m
$\mathbf{F}$, $\mathbf{F}_{\text{AB}}$, $\mathbf{F}_{\text{aero}}$, $\mathbf{F}_{\text{imb}}$	=	generalized force vectors, N
F_b	=	bearing load, N
$f_{\text{AB max}}$	=	maximum autobalancer force, N
$\{\mathbf{h}\}$	=	hub-fixed coordinate frame, $[\mathbf{h}_1, \mathbf{h}_2, \mathbf{h}_3]$
I_i	=	blade cross-sectional-area moment of inertia, m^4
i	=	blade index
J_h	=	hub polar mass moment of inertia, kg-m^2
$\mathbf{K}$, $\mathbf{K}_{\text{blisk}}$, $\mathbf{K}_{\text{AB}}$, $\mathbf{K}_{\text{aero}}$	=	stiffness matrices
k_s	=	bearing-support stiffness, N/m
k_t	=	shaft torsional stiffness, N-m
L_i	=	blade length, m
$\mathbf{M}$, $\mathbf{M}_{\text{blisk}}$, $\mathbf{M}_{\text{AB}}$	=	mass matrices
m_b, m_h	=	ball and hub mass, kg
m_i	=	blade mass per unit length
N, N_m, N_b, N_{ball}	=	number of degrees of freedom, modes, blades, and balls
$\mathbf{N}_{\text{AB}}$, $\mathbf{N}_{\text{ball}}$	=	autobalancer degree-of-freedom mapping matrices
$\mathbf{N}_{\text{blisk}}$, $\mathbf{N}_{\text{hub}}$, $\mathbf{N}_{\text{shaft}}$, $\mathbf{N}_{\text{blade}}$	=	bladed-disk degree-of-freedom mapping matrices
n	=	integer
$\{\mathbf{n}\}$	=	inertially fixed coordinate frame, $[\mathbf{n}_1, \mathbf{n}_2, \mathbf{n}_3]$
P_i	=	material point on ith blade
Q	=	generalized force vector
q, q_{hub}, q_{shaft}, q_{blade}, q_{ball}	=	generalized coordinate vectors
q_{ss}	=	steady-state response
R_b, R_h	=	autobalancer and hub radii, m
$\mathbf{R}_{CB}$, $\mathbf{R}_{OB}$, $\mathbf{R}_{OC}$, $\mathbf{R}_{OP}$	=	position vectors, m
T	=	time, s
T, T_{blisk}, T_{AB}	=	kinetic energy, N-m
T_{vv}, T_{ww}, T_{vw}, T_{wv}	=	hub transfer function matrix elements
t_i	=	blade thickness, m
$u_{\text{blade},i}$	=	local blade displacement vector, m
V	=	strain energy, N-m
$v_{\text{blade},i}$	=	local blade velocity vector, m/s
v_h	=	hub lateral deflection in $\mathbf{h}_2$ direction, m
W	=	virtual work, N-m
w_h	=	hub lateral deflection in $\mathbf{h}_3$ direction, m
w_i	=	elastic blade deflection, m
w_{tip}	=	blade-tip deflection, m
x	=	blade axial coordinate, m
z	=	merged equilibrium solution variable
γ	=	autobalancer force ratio
$\boldsymbol{\eta}_i$, η_{ij}	=	blade modal coordinates, m
θ_{b_i}	=	ball angles at steady state, rad
λ	=	bladed-disk system eigenvalue, rad/s
μ_b	=	autobalancer mass ratio
ξ	=	blade material viscous loss factor, s

Presented as Paper 2334 at the 49th AIAA/ASME/ASCE/AHS/ASC Structures, Structural Dynamics, and Materials Conference, Schaumburg, IL, 7–10 April 2008; received 15 February 2009; revision received 18 June 2009; accepted for publication 27 June 2009.

*Assistant Professor, Aerospace Engineering, Mechanical Aerospace and Biomedical Engineering Department, 606 Dougherty Building; hdesmidt@utk.edu. Member AIAA.

ρ, ρ_b, ρ_{air} = bladed-disk, ball, and air density, kg/m^3
Φ_i, φ_{ij} = blade shape functions
ϕ = bladed-disk hub rotation, rad
ϕ_{b_i} = autobalancer-ball angle, rad
Ψ_i = blade azimuthal location, rad
Ω = bladed-disk rotation speed, rad/s

I. Introduction

BLADE loss in high-speed turbomachinery systems usually results in severe vibration due to synchronous mass and aerodynamic imbalance forces. This paper explores the feasibility of using passive automatic-balancing devices to correct these imbalances in real-time and to passively suppress the vibration. Essentially, automatic-balancing devices (AB or autobalancers) are passive devices consisting of several eccentric masses or balls free to move within a guided circular track that is mounted on a rotor to be balanced [1,2]. At certain rotor speeds, the balancer balls naturally tend to synchronize with the rotor, with appropriate phasing to reduce or cancel the inherent rotor imbalance. This automatic-balancing phenomena occurs as a result of nonlinear dynamic interactions between the balancer balls and lateral vibration of the rotor.

One early experimental study of automatic balancing was by Thearle [1], who characterized the dynamics of a single-ball autobalancer under various rotor imbalance levels. Further, Bovik and Hogfords [2] explored the spin-up and steady-state responses of planar rotor-AB systems. It was shown via numerical integration of the nonlinear equations of motion that complete balancing at supercritical speeds could be achieved by a balancer containing a minimum of two balance masses. Majewski [3] examined the effects of ball rolling resistance and race eccentricity on a rotor-AB system at steady state. It was shown that coulomb frictional effects caused balance-mass positioning errors resulting in residual vibrations. Jinnouchi et al. [4] showed that a single mass autobalancer provided excellent balancing when the rotor was operating at supercritical speeds, but caused increased vibration at subcritical speeds. In an experimental study, Lindell [5] explored the use of an automatic-balancing device to reduce the unbalance vibration in a handheld grinding machine. In this device, several balancing balls were guided to move in an oil-filled circular track mounted in a plane perpendicular to the rotor. Under certain conditions, the balancer balls automatically settled into synchronous orbits that reduced the imbalance vibration. Furthermore, both Rajalingham et al. [6,7] and Chung and Ro [8] used a set of equations in the rotating frame to characterize the stability of the balanced equilibrium configuration for Jeffcott rotors with single- and dual-ball autobalancer devices. It was concluded that increasing bearing-support damping and autobalancer mass ratios tended to decrease the stability of the balanced condition [8].

More recently, several researchers explored the transient response and the global nonlinear behavior of rotor/autobalancer systems. Green et al. [9,10] analyzed limit-cycle behavior for a single-plane rotor fitted with a dual-ball autobalancer. Here, additional nonbalanced subsynchronous limit cycles were found to coexist with the desired synchronous balanced limit cycles. The balanced equilibrium basins of attraction were characterized as a function of ball initial positions. Once the rotor was spun up to its final operating speed, it was shown that these nonbalanced subsynchronous limit cycles could usually be avoided, and the balanced condition reached, by releasing the autobalancer balls from diametrically opposed detent positions [10].

In addition to single-plane rotors, automatic balancing of various nonplanar rotor-AB systems (including out-of-plane tilting, gyroscopic effects, and rotor flexibility) has been investigated [11–16]. Specifically, Chung and Jang [11] and Rajalingham and Bhat [12] explored automatic balancing of a disk-type rotor mounted on a massless cantilevered shaft. A closed-form characteristic equation describing the balanced equilibrium stability of the damped case was obtained using Routh's criteria approach [12]. Furthermore Chao et al. [13,14] analytically and experimentally studied automatic balancing of a vertically oriented optical disk drive spindle. It was shown that through proper choice of autobalancer installation position along the spindle axis, both lateral displacements and tilting-angle vibrations could be simultaneously reduced. Kim et al. [15] concluded that the stability behavior of the AB-spindle system could be adequately predicted by considering a reduced-order model that neglects out-of-plane tilting. For a given operating speed, it was concluded that both the translational and in-plane torsional modes had a significant role in determining the stability of the balanced condition [15].

To understand the effect of rotor flexibility and higher vibration modes on automatic-balancing behavior, DeSmidt [16] analyzed the stability and vibration response of a slender flexible shaft equipped with a dual-mass-autobalancer device. Here, multiple regions of stable automatic balancing were found to exist for rotation speeds between the shaft lateral vibration modes. The rpm width of these balanced regions strongly depended on the axial offset distance between the autobalancer and the imbalance plane. The axial offset tended to either amplify or attenuate the available AB balancing force as a function of rotation speed, thus potentially increasing the maximum effective balancing capacity for a given autobalancer size and weight [16]. Furthermore Ehyaei and Moghaddam [17] reported a similar "partial autobalancing phenomena" in a study conducted on a flexible shaft with multiple autobalancers.

Sohn et al. [18] and Horvath et al. [19] recently explored a dual-pendulum-autobalancer device. By introducing hinge offsets between the rotor center and the pendulum pivot points, it was shown that the pendulum autobalancer can achieve balancing at both sub- and supercritical operating speeds [18]. Furthermore, the pendulum-autobalancer design was shown to be less susceptible to frictional effects than conventional ball-type designs [19]. However, one potential drawback of the pendulum balancer design is that it may not be as weight- and size-efficient as ball-type autobalancers. Extensive experimental studies of single-plane rotor/autobalancer systems have been performed by Lee and Moorham [20] and, more recently, by Lu et al. [21].

Clearly, a key advantage offered by the automatic-balancing approach is the ability to have passive, self-adjusting, rotor imbalance-vibration correction. This investigation explores the feasibility of using a passive automatic-balancing device to correct imbalance in a bladed-disk system in the event of a blade-loss scenario. Previous studies have focused on automatic-balancing behavior of symmetric disk-type rotors subjected to pure mass imbalance. However, in the case of bladed disks (such as turbines and impellers), other important effects in addition to mass imbalance (such as blade aerodynamic loading and blade in-plane vibration modes) become significant. In general, bladed-disk in-plane vibration modes play an increasingly import role for higher-speed operation, and strong torsion/lateral-mode coupling can be induced by an asymmetric blade-out condition. Since the blade aerodynamics and torsion/lateral-mode coupling have not been previously considered in the context of automatic balancing, this study aims to advance the current state of automatic-balancing research by analyzing these effects.

To explore these points, this investigation will study the dynamic stability and vibration response of an imbalanced bladed-disk/rotor/bearing system equipped with a dual-ball autobalancer device (see Figs. 1 and 2).

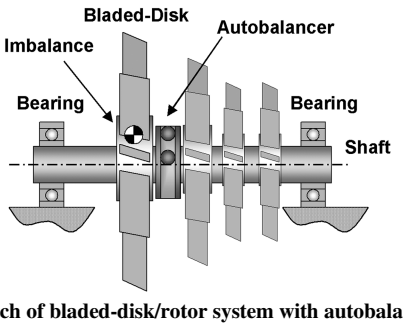

Fig. 1 Sketch of bladed-disk/rotor system with autobalancer device.

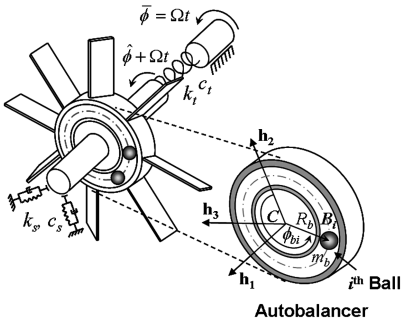

Fig. 2 Bladed-disk/autobalancer system.

This paper solves a coupled set of nonlinear equations in the rotating frame to determine the fixed-point equilibrium conditions and the corresponding steady-state vibration response. The dynamic stability of the bladed-disk/autobalancer system is determined via eigenanalysis of the linearized system about each fixed-point equilibrium configuration. Using this analysis approach, the effects of autobalancer-ball/track damping, blade aerodynamic drag coefficient, and autobalancer mass ratio are each investigated over a range of supercritical operating speeds. The transient response due to a blade-loss scenario is investigated via numerical time-domain integration of the full nonlinear system equations of motion.

II. Bladed-Disk/Autobalancer System Model

To facilitate analysis, the equations of motion for a bladed-disk/autobalancer system are derived in a set of rotating coordinates $\{\mathbf{h}\} = [\mathbf{h_1}, \mathbf{h_2}, \mathbf{h_3}]$, which follow the disk-hub rotation $\phi(t)$ about the $\mathbf{n_1}$ axis of the fixed-frame $\{\mathbf{n}\} = [\mathbf{n_1}, \mathbf{n_2}, \mathbf{n_3}]$ (see Figs. 2 and 3). Here, the model developed and analyzed in this investigation considers only the in-plane dynamics of the flexible bladed-disk/autobalancer system. The blades are modeled as rectangular cross-sectional Euler–Bernoulli beams cantilevered to a rigid rotating disk hub. Figure 3 details the system geometric parameters, deflections, and coordinates for the bladed-disk hub and ith blade.

The position vector locating the hub geometric center C in terms of the lateral deflections $v_h(t)$ and $w_h(t)$ measured from the rotating hub-fixed coordinate system $\{\mathbf{h}\}$ is

$$\mathbf{R}_{OC} = v_h(t)\mathbf{h_2} + w_h(t)\mathbf{h_3} \tag{1}$$

Furthermore, the position vector of a point P_i on the neutral axis of the ith blade in terms of the hub radius R_h blade in-plane elastic deflection $w_i(x, t)$ and blade geometric foreshortening is

$$\mathbf{R}_{OP_i} = \mathbf{R}_{OC} + \left[R_h + x - \frac{1}{2}\int_0^{x_i} w_i'(x,t)^2\,\mathrm{d}x\right]\mathbf{a_{2i}} + w_i(x_i,t)\mathbf{a_{3i}} \tag{2}$$

where prime indicates differentiation with respect to the blade axial coordinate x, and $\{\mathbf{a_i}\}$ is a hub-fixed coordinate system oriented to the ith blade with transformation from $\{\mathbf{n}\}$ to $\{\mathbf{a_i}\}$, given as

$$\begin{bmatrix}\mathbf{a_{2i}}\\ \mathbf{a_{3i}}\end{bmatrix} = \begin{bmatrix}\cos(\phi+\psi_i) & \sin(\phi+\psi_i)\\ -\sin(\phi+\psi_i) & \cos(\phi+\psi_i)\end{bmatrix}\begin{bmatrix}\mathbf{n_2}\\ \mathbf{n_3}\end{bmatrix} \tag{3}$$

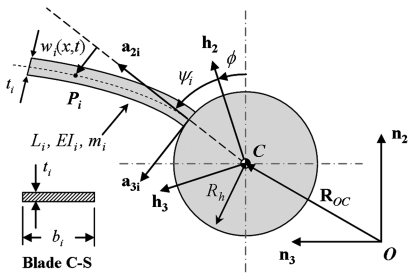

Fig. 3 Hub and blade coordinates (planar dynamics).

where ψ_i is the ith blade azimuth angle. The shaft is assumed to be driven with constant angular speed Ω; hence, the total rotation of the bladed-disk hub is $\phi(t) = \hat{\phi}(t) + \Omega t$, where $\hat{\phi}(t)$ is the shaft elastic twist coordinate. The position vector $\mathbf{R}_{OBi}$ locating the ith balancer ball within the autobalancer can be written

$$\mathbf{R}_{OB_i} = \mathbf{R}_{OC} + \mathbf{R}_{CB_i} \quad \text{with}$$
$$\mathbf{R}_{CB_i} = R_b(\cos[\phi_{b_i}(t)]\mathbf{h_2} + \sin[\phi_{b_i}(t)]\mathbf{h_3}) \quad \text{for } i = 1, 2 \tag{4}$$

where R_b is the ball-track radius and $\phi_{b_i}(t)$ are the ith ball angular positions measured from the $\mathbf{h_2}$ axis. The total system kinetic energy T in terms of the bladed-disk and autobalancer kinetic energies T_{blisk} and T_{AB} is

$$T = T_{\text{blisk}} + T_{\text{AB}} \tag{5a}$$

with

$$T_{\text{blisk}} = \frac{1}{2}m_h\dot{\mathbf{R}}_{OC}\cdot\dot{\mathbf{R}}_{OC} + \frac{1}{2}J_h\dot{\phi}^2 + \sum_{i=1}^{N_b}\frac{1}{2}m_i\int_0^{L_i}\dot{\mathbf{R}}_{OP_i}\cdot\dot{\mathbf{R}}_{OP_i}\,\mathrm{d}x_i \tag{5b}$$

$$T_{\text{AB}} = \sum_{i=1}^{2}\frac{m_b}{2}(\dot{\mathbf{R}}_{OB_i}\cdot\dot{\mathbf{R}}_{OB_i}) \tag{5c}$$

where a dot indicates differentiation with respect to time t, m_h and J_h are hub mass and polar inertia, L_i and m_i are blade length and mass per unit length of the ith blade, N_b is the number of blades, and m_b is the mass of each autobalancer ball. Furthermore, the total system strain energy is

$$V = \frac{1}{2}k_s(v_h^2 + w_h^2) + \frac{1}{2}k_t\hat{\phi}^2 + \sum_{i=1}^{N_b}\frac{1}{2}EI_i\int_0^{L_i} w_i''(x_i,t)^2\,\mathrm{d}x_i \tag{6}$$

where k_s and k_t are the effective lateral bearing support and shaft torsional stiffness values, E is the blade elastic modulus, and I_i is the ith blade area moment of inertia. The system Rayleigh dissipation function is

$$D = \frac{1}{2}c_s(\dot{v}_h^2 + \dot{w}_h^2) + \frac{1}{2}c_t\dot{\hat{\phi}}^2 + \sum_{i=1}^{N_b}\frac{1}{2}\xi EI_i\int_0^{L_i}\dot{w}''_i(x_i,t)^2\,\mathrm{d}x_i + \sum_{i=1}^{2}\frac{1}{2}c_bR_b^2\dot{\phi}_{bi}^2 \tag{7}$$

where c_s and c_t are the bearing lateral support and shaft torsional damping coefficients, ξ is blade material viscous loss factor, and c_b is balancer-ball viscous damping coefficient arising from relative ball/track motion within the autobalancer. The virtual work δW due to blade aerodynamic drag, based on a steady aerodynamic model [22] is expressed as

$$\delta W = -c_d\sum_{i=1}^{N_b}\int_0^{L_i}(v_{\text{blade},i})^2\delta u_{\text{blade},i}\,\mathrm{d}x \tag{8a}$$

where c_d is the blade aerodynamic drag coefficient per unit length that is calculated from the nondimensional drag coefficient C_d together with air density ρ_{air} and blade chord b_i as $c_d = \frac{1}{2}C_d\rho_{\text{air}}b_i$. Furthermore, $v_{\text{blade},i}$ is the local velocity component of the ith blade in the $\mathbf{a_{3i}}$ direction (normal to the blade surface) at station x,

$$v_{\text{blade},i}(x,t) \equiv \dot{\mathbf{R}}_{OP_i}\cdot\mathbf{a_{3i}} \cong (\Omega v_h + \dot{w}_h)\cos\psi_i + (\Omega w_h - \dot{v}_h)\sin\psi_i + (R_h + x)(\dot{\hat{\phi}} + \Omega) + \dot{w}_i \tag{8b}$$

and $\delta u_{\text{blade},i}$ is the corresponding variation of the local blade displacement in the normal direction:

$$\delta u_{\text{blade},i} \equiv \delta[(\mathbf{R}_{OP_i} - \mathbf{R}_{OP_i}|_{v_h=0,w_h=0,\hat{\phi}=0,w_i=0}) \cdot \mathbf{a_{3i}}]$$
$$= \delta w_h \cos\psi_i - \delta v_h \sin\psi_i + (R_h + x)\delta\hat{\phi} + \delta w_i \tag{8c}$$

Next, to obtain the equations of motion, the blade elastic deformations $w_i(x,t)$ are approximated in an assumed modal expansion. The modal expansion of the ith blade is

$$w_i(x_i,t) = \sum_{j=1}^{N_m} \varphi_{ij}(x)\eta_{ij}(t) \tag{9}$$

where $N_m = 3$ is number of elastic blade modes, $\varphi_{ij}(x)$ are the eigenfunctions of a cantilevered Euler–Bernoulli beam [23], and $\eta_{ij}(t)$ is the corresponding modal coordinate of the ith blade. The discretized system equations of motion are then obtained via Lagrange's equations as

$$\frac{\mathrm{d}}{\mathrm{d}t}\left[\frac{\partial T}{\partial \dot{q}}\right] - \frac{\partial T}{\partial q} + \frac{\partial V}{\partial q} + \frac{\partial D}{\partial \dot{q}} = Q \tag{10a}$$

with the $N \times 1$ generalized coordinate vector, where $N = 3 + N_m N_b + 2$ is the total number of degrees of freedom of the bladed-disk/dual-ball autobalancer system:

$$q(t) = [\, q_{\text{hub}}^T(t) \quad q_{\text{shaft}}^T(t) \quad q_{\text{blade}}^T(t) \quad q_{\text{ball}}^T(t)\,]^T \tag{10b}$$

which is composed of

$$q_{\text{hub}}(t) = [\, v_h(t) \quad w_h(t)\,]^T, \qquad q_{\text{shaft}}(t) = \hat{\phi}(t) \tag{10c}$$

$$q_{\text{blade}}(t) = [\, \boldsymbol{\eta}_1^T \quad \boldsymbol{\eta}_2^T \quad \cdots \quad \boldsymbol{\eta}_{N_b}^T\,]^T \tag{10d}$$

$$q_{\text{ball}}(t) = [\, \phi_{b_1}(t) \quad \phi_{b_2}(t)\,]^T \tag{10e}$$

where $\boldsymbol{\eta}_\mathbf{i} = [\eta_{i,1} \cdots \eta_{i,N_m}]^T$ is the $N_m \times 1$ modal coordinate vector for the ith blade, and where the generalized force vector Q satisfies

$$\delta W = Q^T \delta q \tag{11}$$

The resulting nonlinear equations of motion (12) for the bladed-disk/autobalancer in-plane dynamics are

$$\mathbf{M}(v_h, w_h, \phi_{b_1}, \phi_{b_2})\ddot{q} + \mathbf{C}(v_h, w_h, \phi_{b_1}, \phi_{b_2}, \dot{\phi}_{b_1}, \dot{\phi}_{b_2})\dot{q}$$
$$+ \mathbf{K}(\phi_{b_1}, \phi_{b_2})q = \mathbf{F}(\phi_{b_1}, \phi_{b_2}, \dot{\phi}_{b_1}, \dot{\phi}_{b_2}) \tag{12a}$$

where the overall system inertia, damping, and stiffness matrices $\mathbf{M}$, $\mathbf{C}$, and $\mathbf{K}$ and force vector $\mathbf{F}$ are composed of the bladed-disk (blisk) and autobalancer (AB) subsystems as

$$\mathbf{M} = \mathbf{N}_{\text{blisk}}^T \mathbf{M}_{\text{blisk}} \mathbf{N}_{\text{blisk}} + \mathbf{N}_{\text{AB}}^T \mathbf{M}_{\text{AB}}(v_h, w_h, \phi_{b_1}, \phi_{b_2}) \mathbf{N}_{\text{AB}}$$
$$\mathbf{C} = \mathbf{N}_{\text{blisk}}^T [\mathbf{C}_{\text{blisk}} + \mathbf{C}_{\text{aero}}] \mathbf{N}_{\text{blisk}}$$
$$+ \mathbf{N}_{\text{AB}}^T \mathbf{C}_{\text{AB}}(v_h, w_h, \phi_{b_1}, \phi_{b_2}, \dot{\phi}_{b_1}, \dot{\phi}_{b_2}) \mathbf{N}_{\text{AB}}$$
$$\mathbf{K} = \mathbf{N}_{\text{blisk}}^T [\mathbf{K}_{\text{blisk}} + \mathbf{K}_{\text{aero}}] \mathbf{N}_{\text{blisk}} + \mathbf{N}_{\text{AB}}^T \mathbf{K}_{\text{AB}}(\phi_{b_1}, \phi_{b_2}) \mathbf{N}_{\text{AB}}$$
$$\mathbf{F} = \mathbf{N}_{\text{blisk}}^T [\mathbf{F}_{\text{imb}} + \mathbf{F}_{\text{aero}}] + \mathbf{N}_{\text{AB}}^{\text{T}} \mathbf{F}_{\text{AB}}(\phi_{b_1}, \phi_{b_2}, \dot{\phi}_{b_1}, \dot{\phi}_{b_2}) \tag{12b}$$

with corresponding degree-of-freedom mapping matrices $\mathbf{N}_{\text{blisk}}$, $\mathbf{N}_{\text{AB}}$, $\mathbf{N}_{\text{hub}}$, $\mathbf{N}_{\text{shaft}}$, $\mathbf{N}_{\text{blade}}$, and $\mathbf{N}_{\text{ball}}$ defined as

$$\mathbf{N}_{\text{blisk}} = \begin{bmatrix} \mathbf{N}_{\text{hub}} \\ \mathbf{N}_{\text{shaft}} \\ \mathbf{N}_{\text{blade}} \end{bmatrix}, \qquad \mathbf{N}_{\text{AB}} = \begin{bmatrix} \mathbf{N}_{\text{hub}} \\ \mathbf{N}_{\text{shaft}} \\ \mathbf{N}_{\text{ball}} \end{bmatrix} \tag{12c}$$

where

$$q_{\text{hub}} = \mathbf{N}_{\text{hub}} q, \quad q_{\text{shaft}} = \mathbf{N}_{\text{shaft}} q, \quad q_{\text{blade}} = \mathbf{N}_{\text{blade}} q, \quad q_{\text{ball}} = \mathbf{N}_{\text{ball}} q$$

Here, the blisk and AB subsystem matrices and generalized forces in Eq. (12b) are given in the Appendix. Based on the equations of motion (12) and the Appendix, one can see that the autobalancer-ball angles, hub deflections, shaft twisting, and blade motions are inertially coupled, and nonlinear terms arise due to the balancer-ball angles $\phi_{b_i}(t)$.

Since the purpose of this study is to investigate automatic balancing of bladed disks with missing (or partially missing) blades, no assumptions regarding blade symmetry have been made in the model. Thus, system (12) is valid for any general set of blade lengths L_i, mass per unit lengths m_i, and azimuthal arrangements ψ_i for an arbitrary number of blades N_b. The effect of this general blade asymmetry is reflected in the generalized mass-imbalance force vector $\mathbf{F}_{\text{imb}}$ in Eq. (12) and detailed in Eq. (A4). Additionally, the blade aerodynamic drag [Eq. (8)] gives rise to the generalized drag force vector $\mathbf{F}_{\text{aero}}$ as well as to the aerodynamic damping and stiffness matrices $\mathbf{C}_{\text{aero}}$ and $\mathbf{K}_{\text{aero}}$ [see Eqs. (A8–A11)]. The autobalancer produces nonlinear terms involving $\mathbf{M}_{\text{AB}}$, $\mathbf{C}_{\text{AB}}$, and $\mathbf{K}_{\text{AB}}$ as well as the generalized autobalancer force vector $\mathbf{F}_{\text{AB}}$ [see Eqs. (12) and (A12–A15)].

Using Eqs. (A4–A8), the net lateral forces F_{imb} and F_{aero} acting on the hub due to blade mass and aerodynamic asymmetries are

$$F_{\text{imb}} = \Omega^2 \sum_{i=1}^{N_b} m_i L_i \left(\frac{L_i}{2} + R_h\right)[\cos\psi_i \mathbf{h_2} + \sin\psi_i \mathbf{h}_3] \tag{13a}$$

$$F_{\text{aero}} = \frac{c_d \Omega^2}{3} \sum_{i=1}^{N_b} [(L_i + R_h)^3 - R_h^3][\sin\psi_i \mathbf{h_2} - \cos\psi_i \mathbf{h}_3] \tag{13b}$$

These forces have a 90° relative phasing but also have constant magnitude and direction relative to the hub-fixed frame $\{\mathbf{h}\}$. Hence, both are synchronous with the bladed-disk rotation (see Fig. 4). It should also be noted that $\|F_{\text{imb}}\| = 0$ and $\|F_{\text{aero}}\| = 0$ for symmetric blade arrangements. Based on this, the total synchronous imbalance force acting on the hub is

$$F_{\text{hub}} = F_{\text{aero}} + F_{\text{imb}} \tag{14}$$

Furthermore, based on $\mathbf{F}_{\text{AB}}$ [see Eq. (A15)], the net autobalancer force F_{AB} acting on the hub is

$$F_{\text{AB}} = m_b R_b \sum_{i=1}^{2} [(\Omega^2 + \dot{\phi}_{bi}^2)\cos\phi_{bi} \mathbf{h_2} + (\Omega^2 + \dot{\phi}_{bi}^2)\sin\phi_{bi} \mathbf{h}_3] \tag{15}$$

Since the autobalancer balls are free to revolve around to the rotor [i.e., $\phi_{b_i}(t)$ is not constant] F_{AB} is generally not synchronous with the shaft. However, for certain conditions, the autobalancer balls (and hence F_{AB}) do synchronize at steady state. Furthermore, as will be explained in Sec. III, at certain speeds the natural steady-state positions of the balancer balls relative to the rotor are such that they tend to cancel the synchronous hub imbalance force F_{hub}, which is, of course, the desired autobalancing effect.

III. Bladed-Disk/Autobalancer Steady-State Response and Stability Analysis

The governing equations of motion of the bladed-disk/autobalancer system in Eq. (12) are strongly nonlinear in the balancer-ball coordinates $\phi_{b_i}(t)$. Thus, the system cannot be immediately linearized about the trivial equilibrium for analysis. Furthermore, the possibility of multiple fixed-point and limit-cycle equilibria may exist [7,9]. Since previous autobalancer studies have shown that nonsynchronous limit-cycle behavior can typically be avoided by proper choice of initial release positions of the balancer masses [9,10], this study will only focus on characterizing the synchronous steady-state behavior (i.e., the fixed-point equilibria in the rotating frame).

A. Equilibrium Equations

Since the equations have been formulated in the rotating frame and both the mass and aerodynamic imbalance excitations are

synchronous, the possibility of fixed-point equilibria with constant steady-state response q_{ss} exists:

$$\lim_{t\to\infty} \ddot{q}(t) = 0, \qquad \dot{q}(t) = 0 \quad \text{and} \quad q(t) = q_{ss} \tag{16}$$

This implies that the relative autobalancer-ball/track motions have decayed to zero; that is,

$$\lim_{t\to\infty} \ddot{\phi}_{b_i}(t) = 0, \qquad \dot{\phi}_{b_i}(t) = 0 \quad \text{and} \quad \phi_{b_i}(t) = \theta_{b_i} \quad \text{for } i = 1, 2 \tag{17}$$

and thus, at steady state, the balancer balls are rotating synchronously with the bladed-disk hub. By considering Eq. (16) together with Eq. (12) and the Appendix, the overall system at steady state, $\mathbf{K}_{ss}q_{ss} = \mathbf{F}_{ss}$, can be written

$$\begin{bmatrix} \mathbf{K}_{H,H} & \mathbf{0} & \mathbf{K}_{H,B} & \mathbf{0} \\ \mathbf{K}_{S,H} & \mathbf{K}_{S,S} & \mathbf{0} & \mathbf{0} \\ \mathbf{K}_{B,H} & \mathbf{0} & \mathbf{K}_{B,B} & \mathbf{0} \\ \mathbf{K}_{\text{ball},H}(\theta_{b_1}, \theta_{b_2}) & \mathbf{0} & \mathbf{0} & \mathbf{0} \end{bmatrix} \begin{bmatrix} q_{\text{hub}} \\ q_{\text{shaft}} \\ q_{\text{blade}} \\ q_{\text{ball}} \end{bmatrix}\Bigg|_{ss} = \begin{bmatrix} \bar{\mathbf{F}}_{\text{hub}} + \hat{\mathbf{F}}_{\text{hub}}(\theta_{b_1}, \theta_{b_2}) \\ \bar{\mathbf{F}}_{\text{shaft}} \\ \bar{\mathbf{F}}_{\text{blade}} \\ \mathbf{0} \end{bmatrix} \tag{18}$$

where the stiffness matrix and generalized force $\mathbf{K}$ and $\mathbf{F}$ from Eq. (12) have been partitioned corresponding to the hub, shaft, blade, and ball degrees of freedom, and the terms $\bar{\mathbf{F}}$ and $\hat{\mathbf{F}}$ indicate steady-state generalized forces due to the imbalance and aerodynamic loads and the autobalancer, respectively. Based on the structure of Eq. (18) and the Appendix, the steady-state equilibrium equations for the bladed-disk/autobalancer system become

$$\begin{bmatrix} \mathbf{K}_{H,H} & \mathbf{0} & \mathbf{K}_{H,B} \\ \mathbf{K}_{S,H} & \mathbf{K}_{S,S} & \mathbf{0} \\ \mathbf{K}_{B,H} & \mathbf{0} & \mathbf{K}_{B,B} \end{bmatrix} \begin{bmatrix} q_{\text{hub}} \\ q_{\text{shaft}} \\ q_{\text{blade}} \end{bmatrix}\Bigg|_{ss} = \begin{bmatrix} \bar{\mathbf{F}}_{\text{hub}} \\ \bar{\mathbf{F}}_{\text{shaft}} \\ \bar{\mathbf{F}}_{\text{blade}} \end{bmatrix} + \begin{bmatrix} \hat{\mathbf{F}}_{\text{hub}}(\theta_{b_1}, \theta_{b_2}) \\ \mathbf{0} \\ \mathbf{0} \end{bmatrix} \tag{19a}$$

$$\tan\theta_{b_1} = \frac{w_h}{v_h}\bigg|_{ss} \quad \text{and} \quad \tan\theta_{b_2} = \frac{w_h}{v_h}\bigg|_{ss} \tag{19b}$$

Equation (19b) implies that the autobalancer balls are in equilibrium when either

$$\theta_{b_2} = \theta_{b_1} + n\pi \tag{20a}$$

for integer n or

$$v_h = 0 \quad \text{and} \quad w_h = 0 \tag{20b}$$

is satisfied. This leads to three types of equilibrium conditions similar to those observed in previous rigid-rotor/autobalancer studies [5–8]. Specifically, for even n, Eq. (20a) leads to the so-called merged equilibrium condition, in which both balancer balls are together. For odd n, Eq. (20a) leads to a diametrically opposed equilibrium configuration, and Eq. (20b) implies a balanced equilibrium state in which the autobalancer balancing force exactly cancels the rotor imbalance resulting in zero net hub lateral deflections, i.e., $q_{\text{hub}} = \mathbf{0}$. Clearly, the balanced condition is the most desired, since it works to cancel the rotor vibration and bearing loads; however, all three possible cases [Eq. (20)] must be considered. Thus, the steady-state response of the bladed-disk/autobalancer system is obtained by solving Eq. (19a) together with the balanced, merged, and opposed equilibrium conditions. The solution procedure for each of these three cases is explained in Secs. III.B–III.D.

B. Balanced Equilibrium Solution

To proceed with the solution for the balanced case [Eq. (20b)], the zero-hub-deflection condition $q_{\text{hub}} = \mathbf{0}$ is explicitly enforced in Eq. (19a), immediately resulting in

$$\begin{aligned} \mathbf{K}_{H,B}q_{\text{blade}} &= \bar{\mathbf{F}}_{\text{hub}} + \hat{\mathbf{F}}_{\text{hub}}(\theta_{b_1}, \theta_{b_2}) \\ \mathbf{K}_{S,S}q_{\text{shaft}} &= \bar{\mathbf{F}}_{\text{shaft}} \\ \mathbf{K}_{B,B}q_{\text{blade}} &= \bar{\mathbf{F}}_{\text{blade}} \end{aligned} \tag{21}$$

which shows that in the steady-state balanced condition, the shaft twist and blade deflections q_{shaft} and q_{blade} (which are the result of steady aerodynamic blade loading) are decoupled and independent of the autobalancer-ball positions θ_{b_1} and θ_{b_2}. Hence, the balanced bladed-disk response can be directly computed as

$$q_{\text{hub}} = \mathbf{0}, \qquad q_{\text{shaft}} = \mathbf{K}_{S,S}{}^{-1}\bar{\mathbf{F}}_{\text{shaft}}, \qquad q_{\text{blade}} = \mathbf{K}_{B,B}{}^{-1}\bar{\mathbf{F}}_{\text{blade}} \tag{22a}$$

and the corresponding ball angles θ_{b_1} and θ_{b_2} are obtained via the solution of

$$\mathbf{0} = \bar{\mathbf{F}}_{\text{hub}} - \mathbf{K}_{H,B}\mathbf{K}_{B,B}{}^{-1}\bar{\mathbf{F}}_{\text{blade}} + \hat{\mathbf{F}}_{\text{hub}}(\theta_{b_1}, \theta_{b_2}) \tag{22b}$$

where the elements of $\bar{\mathbf{F}}_{\text{hub}}$ are the components of the hub imbalance force vector F_{hub} [Eq. (14)],

$$\bar{\mathbf{F}}_{\text{hub}} \equiv \Omega^2 \sum_{i=1}^{N_b} \left(m_i L_i \left(\frac{L_i}{2} + R_h \right) \begin{bmatrix} \cos\psi_i \\ \sin\psi_i \end{bmatrix} + \frac{c_d}{3}[(L_i + R_h)^3 - R_h^3] \begin{bmatrix} \sin\psi_i \\ -\cos\psi_i \end{bmatrix} \right) \tag{23a}$$

and the elements of $\hat{\mathbf{F}}_{\text{hub}}(\theta_{b_1}, \theta_{b_2})$ are components of the autobalancer force F_{AB} [Eq. (15)] at steady state:

$$\hat{\mathbf{F}}_{\text{hub}}(\theta_{b_1}, \theta_{b_2}) = m_b R_b \Omega^2 \begin{bmatrix} \cos\theta_{b_1} + \cos\theta_{b_2} \\ \sin\theta_{b_1} + \sin\theta_{b_2} \end{bmatrix} \tag{23b}$$

The second term arising in Eq. (22b) represents the change in the synchronous imbalance force as a result of the shift in operation from the nominal imbalanced state to the balanced condition ($v_h = 0$ and $w_h = 0$). Physically, this is a consequence of the following two facts:

1) The bladed-disk center of gravity (c.g.) is a function of the blade deflections.

2) The blade aerodynamic loads (and thus blade deflections) are a function of the lateral hub deflections [see Eq. (8)].

This cross-coupling is represented by the subsystem matrices $\mathbf{K}_{H,B}$ and $\mathbf{K}_{B,H}$ in Eq. (18). Therefore, since the bladed-disk c.g. is ultimately a function of the hub deflection, when the hub deflection is suppressed to zero, $q_{\text{hub}} = \mathbf{0}$, there is a corresponding in a shift in the c.g. location. This c.g. shift alters the effective imbalance load by the amount corresponding to the second term in Eq. (22b). Thus, from Eq. (22b), the total effective synchronous imbalance force $\mathbf{F}_{\text{sync}}$ in the balanced condition is

$$\mathbf{F}_{\text{sync}} = \bar{\mathbf{F}}_{\text{hub}} - \mathbf{K}_{H,B}\mathbf{K}_{B,B}{}^{-1}\bar{\mathbf{F}}_{\text{blade}} \tag{24a}$$

which can be expressed in terms of the system parameters and the terms in the Appendix as

$$\mathbf{F}_{\text{sync}} = \Omega^2 \sum_{i=1}^{N_b} \left(m_i L_i \left(\frac{L_i}{2} + R_h \right) \begin{bmatrix} \cos\psi_i \\ \sin\psi_i \end{bmatrix} + \frac{c_d}{3}[(L_i + R_h)^3 - R_h^3] \begin{bmatrix} \sin\psi_i \\ -\cos\psi_i \end{bmatrix} \right) \cdots + c_d \Omega^4 \sum_{i=1}^{N_b} m_i \mathbf{D}_i [EI_i \mathbf{B}_i + m_i \Omega^2 (\mathbf{C}_i - \mathbf{A}_i)]^{-1} \mathbf{G}_i^T \begin{bmatrix} \sin\psi_i \\ -\cos\psi_i \end{bmatrix} \tag{24b}$$

Here, it should be noted that $\mathbf{F}_{\text{sync}}$ has terms proportional to both Ω^2 and Ω^4. The equation governing the autobalancer-ball equilibrium configuration for the balanced case [Eq. (22b)] becomes

$$\mathbf{F}_{\text{sync}} + m_b R_b \Omega^2 \begin{bmatrix} \cos\theta_{b_1} + \cos\theta_{b_2} \\ \sin\theta_{b_1} + \sin\theta_{b_2} \end{bmatrix} = \begin{bmatrix} 0 \\ 0 \end{bmatrix} \tag{25}$$

which has the solution

$$\theta_{b_1} = \angle \mathbf{F}_{\text{sync}} + \cos^{-1}\left(-\frac{\|\mathbf{F}_{\text{sync}}\|}{2 m_b R_b \Omega^2} \right) \quad \text{and}$$
$$\theta_{b_2} = \angle \mathbf{F}_{\text{sync}} - \cos^{-1}\left(-\frac{\|\mathbf{F}_{\text{sync}}\|}{2 m_b R_b \Omega^2} \right) \tag{26}$$

Thus, Eq. (26) gives the angular positions of the two autobalancer balls when the blade-disk/autobalancer system is operating in the perfectly balanced condition ($v_h = 0$ and $w_h = 0$). Based on Eq. (26) it also apparent that perfect balancing is only possible when $\|\mathbf{F}_{\text{sync}}\| \leq 2 m_b R_b \Omega^2$, where the quantity $f_{\text{AB max}} = 2 m_b R_b \Omega^2$ is the maximum possible balancing force of the dual-ball autobalancer. Based on this, the AB force ratio parameter is defined:

$$\gamma = \frac{\|\mathbf{F}_{\text{sync}}\|}{f_{\text{AB max}}} = \frac{f_{\text{sync}}(\Omega^2, \Omega^4)}{2 m_b R_b \Omega^2} \tag{27}$$

C. Merged Equilibrium Solution

In the merged equilibrium configuration, both balancer balls reach the same angular position, $\theta_b \equiv \theta_{b_1} = \theta_{b_2}$ [see Eq. (20b)]. In this case, the steady-state autobalancer force in Eq. (19a) becomes

$$\hat{\mathbf{F}}_{\text{hub}}(\theta_b) = 2 m_b R_b \Omega^2 \begin{bmatrix} \cos\theta_b \\ \sin\theta_b \end{bmatrix} \tag{28}$$

Using Eq. (28) together with Eq. (19), the lateral hub response in the steady-state merged configuration can be computed as

$$\begin{bmatrix} v_h \\ w_h \end{bmatrix} = \begin{bmatrix} v_{h0} \\ w_{h0} \end{bmatrix} + 2 m_b R_b \Omega^2 \begin{bmatrix} T_{vv} & T_{vw} \\ T_{wv} & T_{ww} \end{bmatrix} \begin{bmatrix} \cos\theta_b \\ \sin\theta_b \end{bmatrix} \tag{29a}$$

where the nominal steady-state hub displacements v_{h0} and w_{h0} are

$$\begin{bmatrix} v_{h0} \\ w_{h0} \end{bmatrix} = \begin{bmatrix} \mathbf{I}_{2\times 2} \\ \mathbf{0} \\ \mathbf{0} \end{bmatrix}^T \begin{bmatrix} \mathbf{K}_{H,H} & \mathbf{0} & \mathbf{K}_{H,B} \\ \mathbf{K}_{S,H} & \mathbf{K}_{S,S} & \mathbf{0} \\ \mathbf{K}_{B,H} & \mathbf{0} & \mathbf{K}_{B,B} \end{bmatrix}^{-1} \begin{bmatrix} \bar{\mathbf{F}}_{\text{hub}} \\ \bar{\mathbf{F}}_{\text{shaft}} \\ \bar{\mathbf{F}}_{\text{blade}} \end{bmatrix} \tag{29b}$$

and where the transfer matrix from the lateral hub force to the hub displacement is

$$\begin{bmatrix} T_{vv} & T_{vw} \\ T_{wv} & T_{ww} \end{bmatrix} = \begin{bmatrix} \mathbf{I}_{2\times 2} \\ \mathbf{0} \\ \mathbf{0} \end{bmatrix}^T \begin{bmatrix} \mathbf{K}_{H,H} & \mathbf{0} & \mathbf{K}_{H,B} \\ \mathbf{K}_{S,H} & \mathbf{K}_{S,S} & \mathbf{0} \\ \mathbf{K}_{B,H} & \mathbf{0} & \mathbf{K}_{B,B} \end{bmatrix}^{-1} \begin{bmatrix} \mathbf{I}_{2\times 2} \\ \mathbf{0} \\ \mathbf{0} \end{bmatrix} \tag{29c}$$

Using Eq. (29a) together with Eq. (19b), the ball angles θ_b in the merged equilibrium must satisfy

$$\tan\theta_b = \frac{w_{h0} + (T_{wv}\cos\theta_b + T_{ww}\sin\theta_b)}{v_{h0} + (T_{vv}\cos\theta_b + T_{vw}\sin\theta_b)} \quad \text{with} \quad \theta_b \equiv \theta_{b_1} = \theta_{b_2} \tag{30}$$

Note that in previous rotor/autobalancer studies [6–8,11] (i.e., rotors without blades), the hub transfer matrix elements T_{vv}, T_{ww}, T_{vw}, and T_{wv} could be explicitly computed in terms of system parameters, and it was found that $T_{vv} = T_{ww}$ and $T_{vw} = -T_{wv}$, which significantly simplifies the solution. However, in the bladed-disk case considered here, with general asymmetric blade arrangements, the hub transfer matrix has no guaranteed symmetry. Therefore, the general solution of Eq. (30) is required. Here, the solution is obtained by first making the following substitution into Eq. (30) in the new variable z, as $\cos\theta_b = z$, $\sin\theta_b = \sqrt{1-z^2}$, and $\tan\theta_b = z/\sqrt{1-z^2}$. After solving for the factor $\sqrt{1-z^2}$ and squaring both sides, the following fourth-order polynomial in z is obtained,

$$c_4 z^4 + c_3 z^3 + c_2 z^2 + c_1 z + c_0 = 0 \tag{31a}$$

with coefficients

$$\begin{aligned} c_0 &= v_{h0}^2 - 2 m_b R_b \Omega^2 T_{vw}^2 \\ c_1 &= 4 m_b R_b \Omega^2 [(T_{vv} - T_{ww}) v_{h0} + T_{vw} w_{h0}] \\ c_2 &= 4 m_b^2 R_b^2 \Omega^4 [(T_{vv} - T_{ww})^2 + 2 T_{vw}(T_{vw} + T_{wv})] - (v_{h0}^2 + w_{h0}^2) \\ c_3 &= 4 m_b R_b \Omega^2 [(T_{ww} - T_{vv}) v_{h0} - (T_{vw} + T_{wv}) w_{h0}] \\ c_4 &= -4 m_b^2 R_b^2 \Omega^4 [(T_{vv} - T_{ww})^2 + (T_{vw} + T_{wv})^2] \end{aligned} \tag{31b}$$

After numerically solving for the roots z_i ($i = 1, \ldots, 4$) of Eq. (31) and retaining only those roots satisfying both $\text{Im}[z_i] = 0$ and $|z_i| \leq 1$, the merged ball-angle solution θ_b is obtained as $\theta_b = \cos^{-1} z_i$.

D. Opposed Equilibrium Solution

In the opposed equilibrium configuration, the balancer balls become diametrically opposed, i.e., $\theta_{b_2} = \theta_{b_1} + \pi$ [see Eq. (20b)]. In this case, the steady-state autobalancer force in Eq. (19a) becomes zero and the only net effect of the autobalancer on the bladed-disk system is the added mass $2m_b$ of the two balancer balls [which is accounted for in the matrix $\mathbf{K}_{H,H}$ (see Eq. (18) and the Appendix)]. Thus, conditions (19b) and (20b) are satisfied if and only if

$$\theta_{b_1} = \tan^{-1}\left[\frac{w_{h0}}{v_{h0}} \right] \quad \text{and} \quad \theta_{b_2} = \tan^{-1}\left[\frac{w_{h0}}{v_{h0}} \right] + \pi \tag{32}$$

where v_{h0} and w_{h0} are computed from Eq. (29b). This implies that the balls line up on both ends of the bladed-disk lateral response axis where the bladed-disk response phase angle (relative to the hub-fixed frame $\{\mathbf{h}\}$) is

$$\phi_0 = \tan^{-1}\left[\frac{w_{h0}}{v_{h0}} \right] \tag{33}$$

E. Local Stability Analysis

To assess the physical significance of the balanced, merged, and opposed cases described in Secs. III.B–III.D, the local asymptotic stability behavior of the bladed-disk/autobalancer system is investigated in the vicinity of each steady-state equilibrium configuration via a perturbation and linearization approach. After considering small perturbations $\hat{q}(t)$ about a particular equilibrium configuration q_{ss}, the perturbed system response is

$$q(t) = q_{ss} + \hat{q}(t) \tag{34}$$

Substituting Eq. (34) into the full nonlinear dynamic system (12a) and dropping higher-order terms results in a set of linearized equations of motion about each configuration q_{ss}, denoted as

$$\hat{\mathbf{M}}(q_{ss})\ddot{\hat{q}}(t) + \hat{\mathbf{C}}(q_{ss})\dot{\hat{q}}(t) + \hat{\mathbf{K}}(q_{ss})\hat{q}(t) = 0 \tag{35}$$

Upon defining the state vector $\mathbf{x}(t) = [\,\hat{q}^T \quad \dot{\hat{q}}^T\,]^T$, Eq. (34) is transformed into first order form

$$\dot{\mathbf{x}} = A(q_{ss})\mathbf{x} \quad \text{with}$$

$$A(q_{ss}) = \begin{bmatrix} 0 & I \\ -\hat{\mathbf{M}}^{-1}(q_{ss})\hat{\mathbf{K}}(q_{ss}) & -\hat{\mathbf{M}}^{-1}(q_{ss})\hat{\mathbf{C}}(q_{ss}) \end{bmatrix} \tag{36}$$

The local stability is then determined by assessing the eigenvalues, λ, of the system

$$[I\lambda_i - A(q_{ss})]\mathbf{x}_i = 0 \quad \text{for } i = 1, 2, \ldots, 2N \tag{37}$$

where the steady-state equilibrium configuration q_{ss} is considered stable if $\text{Re}[\lambda_i] < 0$ for $i = 1, 2, \ldots, 2N$.

IV. Bladed-Disk/Autobalancer Steady-State Response and Stability Results

Using the bladed-disk/autobalancer model derived in Sec. II and the analysis methodology developed in Sec. III, this section explores the stability and steady-state vibration response of a particular eight bladed-disk/dual-ball autobalancer system. Specifically, the effects of blade aerodynamic drag c_d, relative AB ball/track damping c_b, and AB balancer-ball mass m_b are each assessed over a wide rpm operating range for a blade-out condition. The bladed-disk and autobalancer parameters used in this investigation are summarized in Tables 1 and 2. Furthermore, the assumed single blade-out condition is depicted in Fig. 5, in which the blade-length loss parameter ($0 \le \varepsilon_b \le 1$) is defined as the fraction of blade-length lost from a particular blade.

The dual-ball autobalancer used in this study is sized for an assumed worst case scenario of losing one complete blade (i.e., $\varepsilon_b = 1$). To ensure zero residual imbalance, the worst case imbalance load should be less than the maximum possible autobalancer balancing force $f_{\text{AB max}} = 2m_bR_b\Omega^2$. using Eq. (14) to estimate the maximum imbalance load, the dual-ball autobalancer sizing criteria becomes

$$2m_bR_b \ge \sqrt{\frac{m_i^2}{4}[(L_i + R_h)^2 - R_h^2]^2 + \frac{c_d^2}{9}[(L_i + R_h)^3 - R_h^3]^2} \tag{38a}$$

with blade mass per unit length $m_i = \rho b_i t_i$ and where the autobalancer-ball diameter is determined from

$$D_b = \left[\frac{6m_b}{\rho_b \pi}\right]^{1/3} \tag{38b}$$

By considering the case in which the autobalancer and the bladed-disk hub have the same radius (i.e., $R_h = R_b$) along with the parameters from Tables 1 and 2, the sizing criteria (38) yield the minimum balancer-ball diameter (rounded up to the nearest integer) of $D_b = 13$ mm.

Table 2 Autobalancer parameters

Parameter	Value	Units
Number of AB balls N_{ball}	2	——
AB ball-track radius R_b	25	mm
AB ball diameter D_b	13	mm
AB ball density ρ_b	7870	kg/m^3
AB ball mass m_b	0.00905	kg
AB ball-track damping c_b	Various[a]	kg/s

[a]Various values used in the analysis

Figure 6 shows the natural frequency maps of the bladed-disk system versus shaft rotation speed, Ω, for the undamaged case (Fig. 6a) and for the missing-blade case (Fig. 6b). Here, the modes primarily associated with blade deflections increase with Ω due to centripetal stiffening. Furthermore, the natural frequency associated with hub lateral motion due to bearing deflection (70.1 Hz at $\Omega = 0$ rpm) is split into the so-called forward and backward modes [24], which is a consequence of the fact that the equations of motion have been formulated in the rotating frame. Physically, the lateral natural frequencies are essentially constant when measured in the fixed-frame, however, relative to the rotating frame, the lateral oscillation frequency of the bladed-disk hub is shifted by the amount $\pm\Omega$. One can refer to Bucher and Ewins [24] for further discussion on this topic. Comparing Figs. 6a and 6b shows that the missing blade results in a slight shift in some modal frequencies, but more significantly, the blade pattern asymmetry causes the system to become dynamically unstable over two operating-speed ranges.

To investigate automatic-balancing behavior of bladed disks, the steady-state response with and without the autobalancer is detailed in Figs. 7–12. Specifically, Figs. 7 and 8 show the magnitude of the steady-state bearing load

$$\|F_b\| = k_s\sqrt{v_h^2 + w_h^2} \tag{39}$$

and the blade elastic tip deflections $w_{\text{tip}} = w_i(L_i)$ versus rotor speed for the missing-blade case, with and without the autobalancer. In the case without autobalancing, Fig. 7a shows that the bearing load peaks at about $\|F_b\| \approx 1550$ N near the first lateral-mode crossing speed ($\Omega \approx 4530$ rpm) and then attenuates to a relatively constant value of about $\|F_b\| \approx 90$ N at supercritical speeds. In addition to exciting the bearing load, the aerodynamic and mass imbalances induced by the missing blade result in an asymmetric blade response pattern as illustrated by the steady-state blade-tip deflections in Fig. 7b. Here, near the first lateral-mode crossing speed, ($\Omega \approx 4530$ rpm), both blade leading ($w_{\text{tip}} > 0$) and lagging ($w_{\text{tip}} < 0$) occur. Furthermore, at

Table 1 Bladed-disk parameters

Parameter	Value	Units
Hub radius R_h	25.0	mm
Hub mass m_h	0.704	kg
Hub polar inertia J_h	2.991×10^{-5}	kg-m^2
Number of blades N_b	8	——
Blade azimuth angles ψ_i	$n\pi/4$ ($n = 0$ to 8)	rad
Blade length L_i	80.0 (nominal)	mm
Blade length loss fraction ε_b	Various[a]	——
Blade width b_i	20	mm
Blade thickness t_i	1.5	mm
Blade density ρ	2800	kg/m^3
Blade elastic modulus E	75	GPa
Blade-loss factor ξ	1.0×10^{-5}	s
Blade drag coefficient c_d	Various[a]	kg/m^2
Bearing support stiffness k_s	2.416×10^4	N/m
Bearing support damping c_s	2.133	kg/s
Shaft torsional stiffness k_t	1035.6	N-m
Shaft torsional damping c_t	0.0205	N-m-s

[a]Various values used in the analysis.

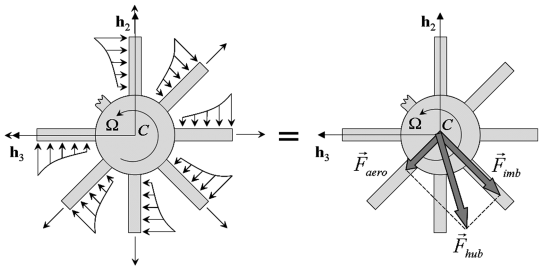

Fig. 4 Synchronous hub forces induced by blade aerodynamic and mass asymmetries.

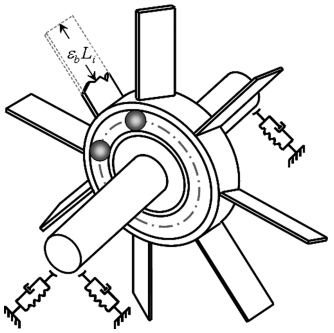

Fig. 5 Blade-out condition; blade-length loss parameter ε_b.

supercritical speeds, all blade deflections become lagging as result of aerodynamic drag. The amount of lag for a particular blade is a function of its azimuthal location, ψ_i, relative to the missing blade. The two shaded regions (regions I) in Fig. 7 highlight the unstable operating-speed zones of the bladed disk (also see Fig. 6).

When the bladed disk is fitted with an automatic-balancing device, Fig. 8a shows that the autobalancer achieves perfect balancing (i.e., $v_h = 0$, $w_h = 0$, and $\|F_b\| = 0$) at operating speeds sufficiently above the first lateral-mode crossing. However, at subcritical speeds, the autobalancer increases the bearing load (and lateral response) (see Fig. 10a for a comparison). Additionally, the steady-state blade-tip deflections of the bladed-disk/autobalancer system are shown in Fig. 8b. At speeds at which autobalancing is achieved, the blades all have an identical lag deflection response. Furthermore, comparing the blade responses in Fig. 7b with Fig. 8b shows that the autobalancer has the effect of reducing the maximum blade deflection. This is also seen in Fig. 10b which plots the maximum blade-tip deflection for the case with and without the autobalancer. The result also shows that the autobalancer introduces a new instability zone (shaded regions II in Figs. 8–10) starting just above the first lateral-mode crossing speed. Note, the instability zones inherent to the original bladed-disk (regions I) remain essentially unchanged by the presences of the autobalancer.

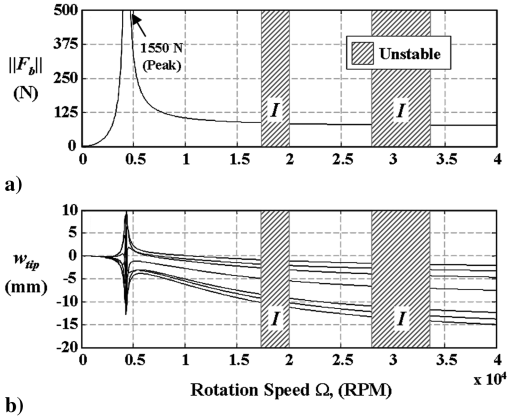

Fig. 7 Bladed-disk response without autobalancer vs rotation speed for one missing blade, $c_d = 0.05$ kg/m^2: a) hub bearing load and b) blade-tip deflections.

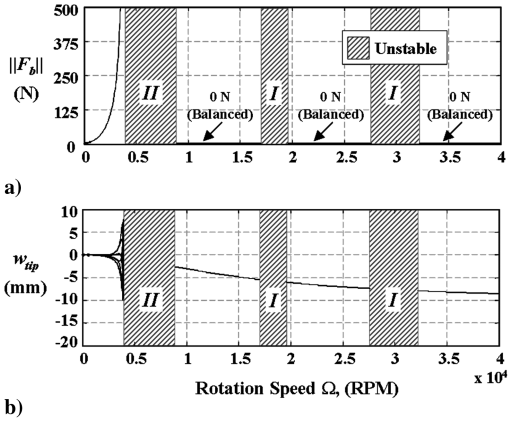

Fig. 8 Bladed-disk response with autobalancer vs rotation speed for one missing blade, $c_d = 0.05$ kg/m^2, $c_b = 0.02$ kg/s, and $D_b = 13$ mm: a) hub bearing load and b) blade-tip deflections.

More insight into the response is gained by examining the autobalancer balancer-ball positions at steady state, which are displayed in Fig. 9. At subcritical rpm, the two balancer balls become in phase with each other and together they synchronize with the bladed disk's rotation. This corresponds to the merged ball equilibrium configuration discussed in Secs. III.A and III.C. At subcritical rpm, the balancer balls become in phase with the net bladed-disk imbalance, resulting in increased lateral vibration and bearing load (see Fig. 8a). As Ω approaches the first lateral-mode crossing speed ($\Omega \approx 4530$ rpm), the steady-state ball positions become out of phase with the bladed-disk imbalance. For a range of Ω just above the first lateral-mode crossing, the system becomes

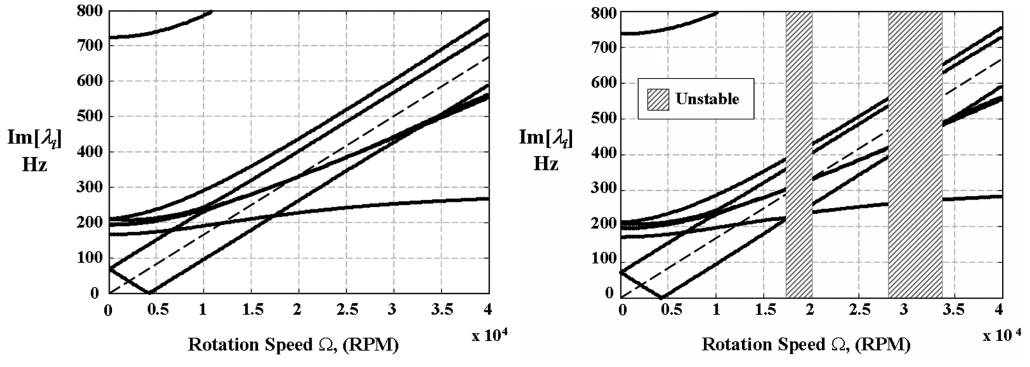

Fig. 6 Bladed-disk natural frequencies vs rotation speed, $c_d = 0.05$ kg/m: a) undamaged case and b) one missing blade.

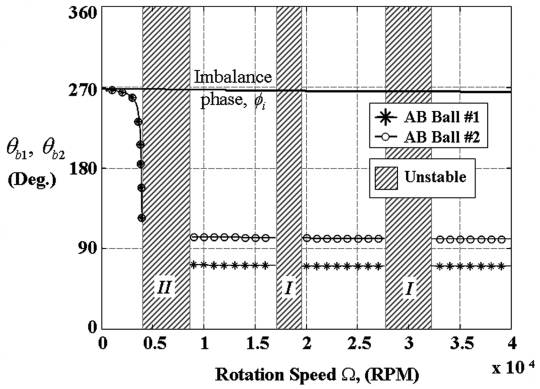

Fig. 9 Steady-state autobalancer-ball positions vs rotation speed for one missing blade, $c_d = 0.05$ kg/m^2, $c_b = 0.02$ kg/s, and $D_b = 13$ mm.

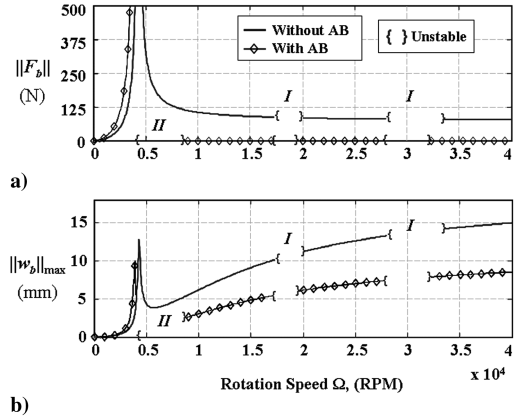

Fig. 10 Bladed-disk response comparison; one missing blade, $c_d = 0.05$ kg/m^2, $c_b = 0.02$ kg/s, and $D_b = 13$ mm: a) hub bearing load and b) maximum blade elastic deflection.

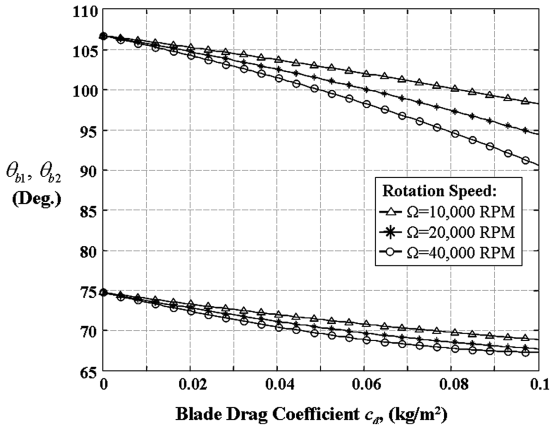

Fig. 11 Autobalancer-ball equilibrium angles for balanced operation vs blade drag coefficient at three rotation speeds with one missing blade, $c_b = 0.02$ kg/s, and $D_b = 13$ mm.

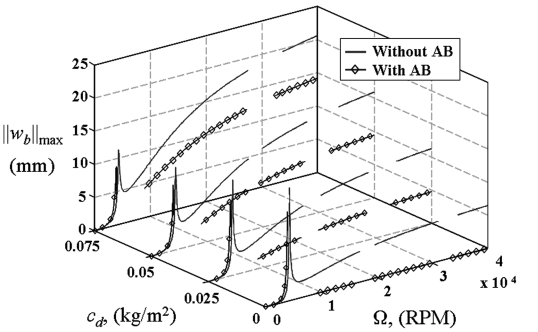

Fig. 12 Maximum blade elastic deflection vs rotation speed for various values of blade drag coefficient with one missing blade, $c_b = 0.02$ kg/s, and $D_b = 13$ mm.

unstable (i.e., region II). In the context of the linearized analysis method presented in Sec. III, the unstable region II corresponds to an rpm range in which no stable fixed-point balancer-ball equilibria are found to exist. In other words, for Ω operating in region II, the balancer balls do not tend to synchronize with the bladed disk at steady state [i.e., $\dot{\phi}_{b_i}(t) \neq 0$ as $t \to \infty$], but rather, they keep moving relative to the rotor (nonsynchronous behavior) in some type of limit cycle. The balancer-ball behavior in regions I and II cannot be predicted from linearized analysis. Therefore, this nonsynchronous behavior in these regions will be further explored via numerical time-domain simulation of the full nonlinear equations in Sec. V. At supercritical speeds outside regions I and II, stable automatic balancing occurs. Here, the two balancer balls settle into different positions, with one ball greater than 180° relative to the imbalance and the other less than 180° relative to the imbalance, such that the net autobalancer force exactly cancels the bladed-disk aerodynamic and mass imbalance (see Figs. 8 and 9). The angular separation between balancer balls is a measure of the remaining autobalancing authority. Obviously, for the limiting case of diametrically opposed balancer balls (i.e., $|\theta_{b2} - \theta_{b1}| = \pi$), the autobalancing force is zero. Furthermore, the maximum force that the autobalancer can provide is $f_{AB\max} = 2m_b R_b \Omega^2$, which occurs when both balancer balls are in phase (i.e., $|\theta_{b2} - \theta_{b1}| = 0$).

In the case of bladed disks, the imbalance that must be counteracted by the autobalancer is due to both mass and aerodynamic asymmetries resulting from the missing blade(s). The results shown thus far are for a single level of blade aerodynamic drag, $c_d = 0.05$ kg/m^2. Figures 11 and 12 illustrate the effect of different drag coefficient values c_d on the bladed-disk/autobalancer response.

Figure 11 shows the balancer-ball equilibrium angles versus c_d at three different operating speeds. As the drag level c_d increases, the balancer-ball angular separation is reduced, indicating that more balancing force is required by the autobalancer to counteract the aerodynamic portion of the imbalance. Furthermore, more subtly, Fig. 11 also shows that for a given level of drag $c_d > 0$, the amount of angular separation $|\theta_{b2} - \theta_{b1}|$, and hence the remaining autobalancing authority diminishes for larger values of Ω. Therefore, in the absence of aerodynamic effects (pure mass-imbalance case), the AB has the same effective balancing capacity for all operating speeds. However, when an aerodynamic imbalance exists, the effective balancing capacity of the AB decreases with increasing rpm. This means that an autobalancer that is sized to completely cancel imbalance at a lower speed may saturate at higher speeds. This does not occur for a pure mass imbalance, since both imbalance and autobalancing forces are proportional to Ω^2, and hence the operating-speed effects cancel [2–8]. However, when aerodynamic imbalance is present in a bladed disk, the synchronous imbalance force $\mathbf{F}_{\text{sync}}$ [Eq. (24)] has terms proportional to both Ω^2 and Ω^4. Thus, at higher speeds, the imbalance tends to become larger relative to the maximum balancing capacity of a given autobalancer design. This is an important new result that did not arise in previous autobalancing investigations.

Furthermore, Fig. 12 shows the maximum steady-state blade deflection response versus speed for several values of the blade drag coefficient with and without an autobalancer for the missing-blade case. This result shows that the automatic balancer is beneficial over the range of drag levels, since it reduces the maximum blade-tip deflections compared with the no-autobalancer case.

One important autobalancer design parameter is the ball/track viscous damping c_b, which tends to damp out ball motions relative to the rotor. In other words, c_b resists nonsynchronous ball motions [see Eq. (7)] and is typically accomplished via some form of oil within the AB track [2]:

$$c_b^* = \min_{\substack{v_h = 0,\, w_h = 0 \\ \text{(balanced)}}} [c_b] \tag{40}$$

The contour plots in Figs. 13–15 explore the minimum ball/track viscous damping c_b^* [Eq. (40)], required for stable automatic balancing. In these figures, the shaded areas correspond to regions in which stable automatic balancing of the bladed disk occurs (i.e., when $v_h \to 0$ and $w_h \to 0$ as $t \to \infty$), and the areas with diagonal lines indicate regions in which automatic balancing is not possible, regardless of the AB ball/track damping amount c_b.

In particular, Fig. 13 shows c_b^* versus operating speed Ω and blade drag coefficient c_d. Here, it is shown that autobalancing of the bladed disk is only possible for Ω above the first lateral-mode crossing speed, regardless of blade drag level. Furthermore, for supercritical rpm, with the exception of the two unstable operating-speed ranges ***b*** and ***c*** in Fig. 13, the AB ball damping required for stable automatic balancing tends to increase with blade drag level c_d and tends to decrease with operating speed Ω. In this regard, since increasing blade drag increases the required AB ball damping, blade drag essentially has a destabilizing effect on the automatic-balancing phenomena. However, at the same time, blade drag also has stabilizing effects on the bladed disk over certain narrow speed ranges. Specifically, the unstable rpm range in Fig. 13 region ***b*** vanishes for sufficiently large ($c_d > 0.65$) blade drag coefficient values.

Next, Fig. 14 illustrates the effects of balancer-ball mass on bladed-disk autobalancing behavior. Specifically, Fig. 14 shows c_b^* versus the operating speed Ω and the AB ball mass ratio μ_b:

$$\mu_b = \frac{m_b}{m_h + \sum_{i=1}^{N_b} m_i L_i} \tag{41}$$

The dashed line indicating a ball diameter of $D_b = 13$ mm in Fig. 14 is the design point determined from the autobalancer sizing equation (38), which is used in all other computational results in this paper. The design level $D_b = 13$ mm ($\mu_b = 0.086$) corresponds to the minimum ball diameter (rounded up to the nearest integer), which can completely balance one missing blade ($\varepsilon_b = 1$). Thus, values of $D_b > 13$ mm ($\mu_b > 0.086$) offer excess balancing capacity and thus correspond to excess weight. Furthermore, it is found that increasing μ_b tends to reduce the stability of automatic balancing for Ω just above the first lateral-mode crossing speed. For example, Fig. 14 shows that for $\mu_b = 0.1$ automatic balancing can be achieved for speeds as low as $\Omega \approx 7000$ rpm; however, if the mass ratio is increased to $\mu_b = 0.14$, then automatic balancing cannot be achieved until at least $\Omega \approx 10,000$ rpm.

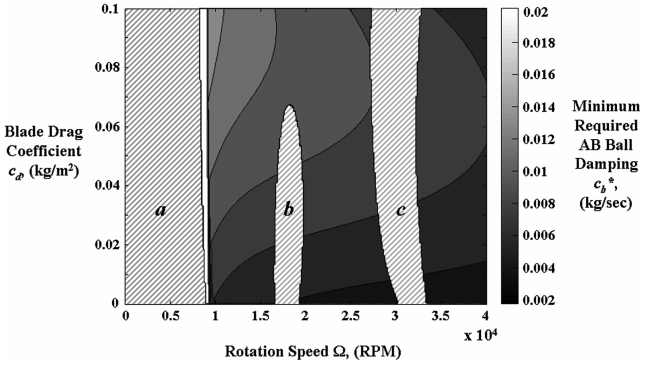

Fig. 13 Minimum AB ball damping required for stable automatic balancing vs rotation speed and blade drag coefficient for one missing blade, $D_b = 13$ mm.

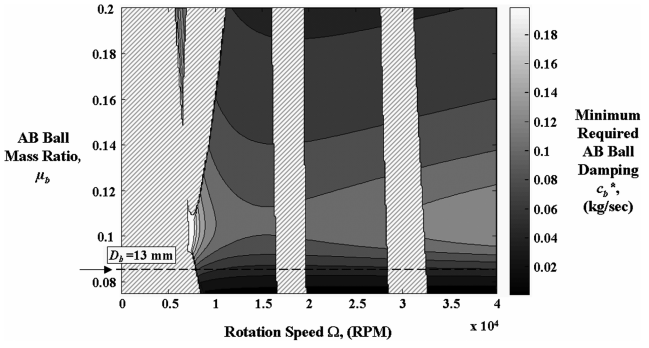

Fig. 14 Minimum AB ball damping required for stable automatic balancing vs rotation speed and AB ball mass ratio for one missing blade, $c_d = 0.05$ kg/m².

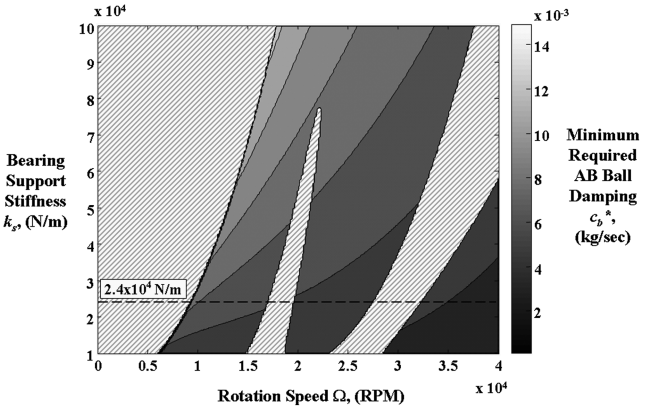

Fig. 15 Minimum AB ball damping required for stable automatic balancing vs rotation speed and bearing stiffness for one missing blade, $c_d = 0.05$ kg/m², and $D_b = 13$ mm.

Figure 14 also shows that the level c_b^* required for automatic balancing reaches a maximum value for intermediate values of μ_b. Hence, the best autobalancer design from both weight and stability points of view is one that keeps μ_b as low as possible based on sizing equation (38).

Figure 15 explores the effect of the bearing-support stiffness k_s on bladed-disk autobalancing behavior. As k_s is increased, so do the bladed-disk lateral natural frequencies. As a result, Fig. 15 shows that the minimum operating speed at which autobalancing occurs increases with k_s. Furthermore, it is also observed that the minimum balancer-ball damping c_b required for stable autobalancing is larger, because of the higher values of support stiffness k_s. This is partly due to the increased level of lateral bearing-support damping c_s, which naturally accompanies k_s in a proportional manner. In other words, there is a minimum ratio of internal (autobalancer) to external (support) damping c_b/c_s that must be satisfied for automatic balancing to occur.

V. Bladed-Disk/Autobalancer Blade-Loss Time-Domain Simulation Results

To investigate the transient response of the bladed-disk/autobalancer system and to validate the stability and steady-state analysis developed and explored in Secs. III and IV, a time-domain simulation via direct numerical integration of the full nonlinear equations of motion (12) is performed. The system equations (12) are implemented in a MATLAB® PC environment, and the response is computed using the adaptive time-step ordinary differential equation solver command `ode45.m`. In this study, a blade-loss event is simulated by removing the blade degrees of freedom associated with the lost blade at a prescribed time in one time step. Using this approach, the response to a multiple-blade-loss scenario described in Table 3 is computed. In this scenario, the bladed disk has a constant operating speed and is initially undamaged. At $t = 0.5$ s, one blade (blade 3) is lost, followed by another (blade 4) at $t = 2.0$ s. Since the two lost blades are adjacent, this represents the most severe imbalance condition for a double-blade-loss situation. The simulation results are given in Figs. 16–18.

In this simulation, the bladed-disk operating conditions are $\Omega = 15,000$ rpm and $c_d = 0.05$ kg/m², and the autobalancer parameters

Table 3 Simulated blade-loss scenario[b]

	Undamaged	First blade loss	Second blade loss
Time range	$0 \le t < 0.5$	$0.5 \le t < 2.0$	$2.0 \le t \le 3.5$
Excitation condition	Hub imbalance[a] ($e_{cc} = 1 \times 10^{-7}$ m)	Hub imbalance[a] ($e_{cc} = 1 \times 10^{-7}$ m)	Hub imbalance[a] ($e_{cc} = 1 \times 10^{-7}$ m)
Blades removed	——	Blade 3 ($\psi_3 = \pi/2$)	Blade 3 ($\psi_3 = \pi/2$) and blade 4 ($\psi_4 = 3\pi/4$)

[a]A small initial hub imbalance due to manufacturing tolerance is assumed.
[b]Simulation results are given in Figs. 16–18.

are $c_b = 0.02$ kg/s and $D_b = 13$ mm. For this set of values, the equilibrium and stability analysis results from Sec. IV (see Figs. 8 and 13) predict stable automatic-balancing behavior. Figures 16a and 16b show the bearing load and the blade-tip deflection of the bladed disk without the automatic balancer, and Figs. 17 and 18 show the response of the combined bladed-disk/AB system (i.e., with the autobalancer).

As to be expected, after each blade loss, the system experiences a large transient response due to the sudden increase in imbalance. In the no-autobalancer case, after the first blade is lost, the transient bearing load peaks at $\|F_b\| = 421$ N and then settles down to a steady state of about $\|F_b\| = 90$ N. After the second blade is lost, the transient bearing load peaks again at $\|F_b\| = 548$ N and then settles down to a steady value of about $\|F_b\| = 178$ N (see Fig. 16a). In comparison, when the autobalancer is included, after the first blade is lost, the transient bearing load peaks at $\|F_b\| = 382$ N (9.2 % reduction) and then is suppressed to zero, $\|F_b\| = 0$ N (100% reduction), by the action of the autobalancer. Furthermore, after the second blade is lost, the bearing load peaks at $\|F_b\| = 406$ N (26% reduction) and then settles down to about $\|F_b\| = 68$ N (62% reduction) (see Fig. 17a). Thus, the autobalancer reduces both the transient and steady-state lateral responses. Furthermore, the residual blade-tip deflections with the autobalancer (Fig. 17b) have significantly less magnitude than with the no-autobalancer case (Fig. 16a). Note that blade responses are all nominally negative due to aerodynamic drag.

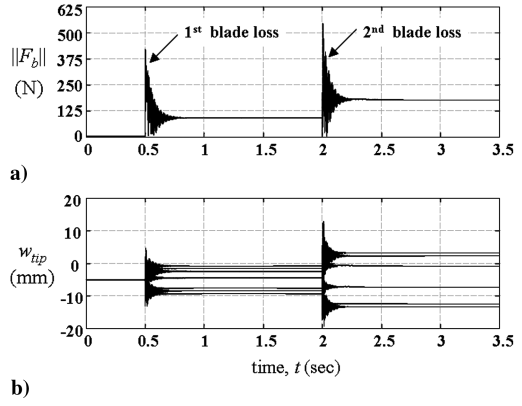

Fig. 16 Bladed-disk response for double-blade-loss scenario (without AB), $\Omega = 15,000$ rpm, and $c_d = 0.05$ kg/m^2: a) hub bearing load and b) blade-tip deflections.

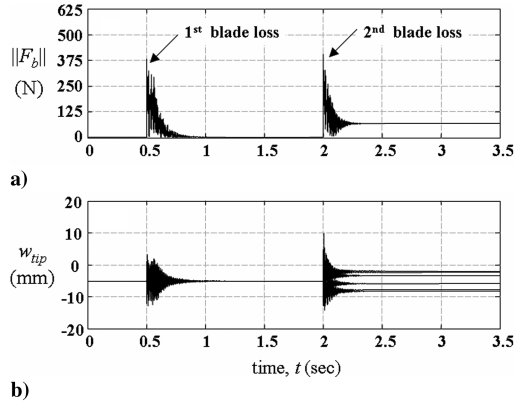

Fig. 17 Bladed-disk response for double-blade-loss scenario (with AB), $\Omega = 15,000$ rpm, $c_d = 0.05$ kg/m^2, $c_b = 0.02$ kg/s, and $D_b = 13$ mm: a) hub bearing load and b) blade-tip deflections.

Further insight can be gained by examining the response of the autobalancer-ball angles in Fig. 18. Here, before the blade loss, the autobalancer balls are arrayed in an essentially diametrically opposed configuration at approximately 90 and 270° to cancel the initial (very small) hub imbalance (see Table 3). After the first blade-loss event, the balls automatically settle into new steady-state positions that cancel the imbalance resulting from the mass and aerodynamic asymmetries. Since the autobalancer has been sized to completely balance the loss of one blade [via Eq. (38) with ball diameter rounded up to the nearest-millimeter integer, $D_b = 13$ mm], there is some remaining balancing capacity after the first blade is lost. This is indicated by the nonzero angle of separation between the balancer balls at steady state (Fig. 18 for $1.5 < t < 2.0$ s). Next, after the second blade is lost, the balancer balls once again move to new positions to counteract the new synchronous imbalance. However, in this case, after the second blade is lost, the imbalance force exceeds the maximum balancing capacity of the autobalancer (i.e., $\|\mathbf{F}_{\text{sync}}\| > 2m_b R_b \Omega^2$) and the position of the balancer balls become merged 180° out of phase with the imbalance (Fig. 18 for $t > 2.5$ s). Furthermore, the bearing load after the second blade-loss event is not completely suppressed to zero (Fig. 17a); however, it is significantly less that the no-autobalancer case (Fig. 16a).

Figures 19 and 20 demonstrate a case in which the analyses in Secs. III and IV predict unstable autobalancing behavior. Specifically, when the blade-disk rotation speed operates in a range just above the first lateral-mode crossing speed, the analysis predicts that no stable fixed-point balancer-ball equilibria exist (see region II in Figs. 8–10). Referring to Fig. 8, one such speed at which this occurs is $\Omega = 7500$ rpm. At this operating speed, Fig. 19 shows the bladed-disk response to a single blade loss without the automatic balancer. In this case, after a is blade lost, the system reaches a new stable fixed-point equilibrium configuration (see Fig. 19) with

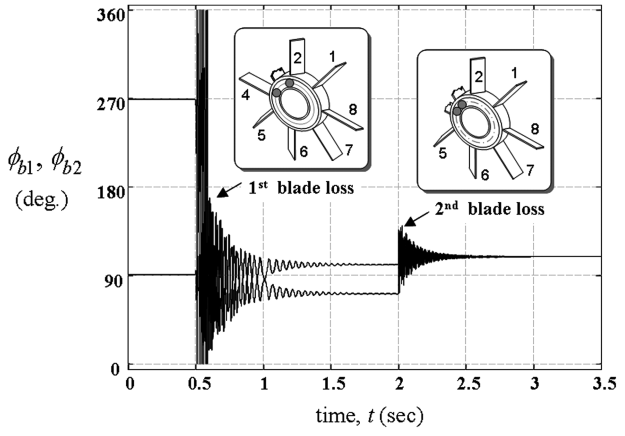

Fig. 18 Autobalancer-ball positions for double-blade-loss scenario, $\Omega = 15,000$ rpm, $c_d = 0.05$ kg/m^2, $c_b = 0.02$ kg/s, and $D_b = 13$ mm.

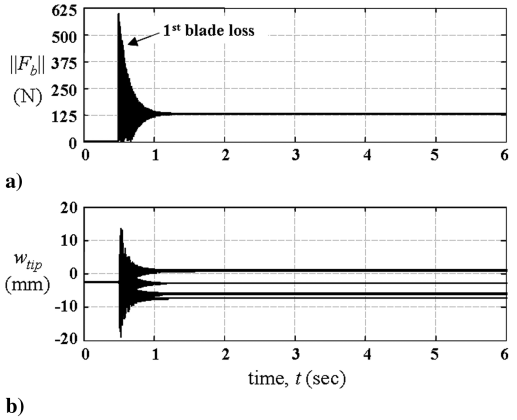

Fig. 19 Bladed-disk response for single-blade-loss scenario (without AB), $\Omega = 7500$ rpm, and $c_d = 0.05$ kg/m^2: a) hub bearing load and b) blade-tip deflections.

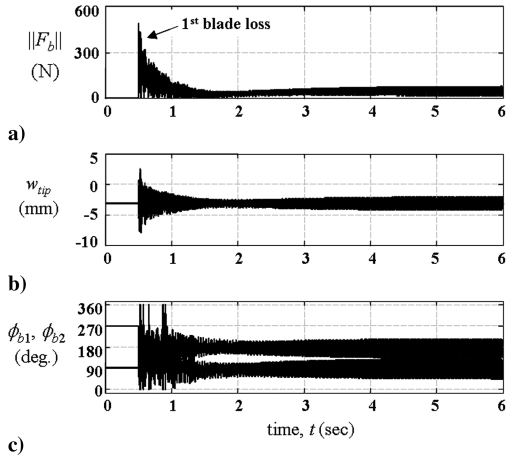

Fig. 20 Bladed-disk response for single-blade-loss scenario (with AB), $\Omega = 7500$ rpm, $c_d = 0.05$ kg/m^2, $c_b = 0.02$ kg/s, and $D_b = 13$ mm: a) hub bearing load, b) blade-tip deflections, and c) autobalancer-ball positions.

$\|F_b\| = 126$ N, which, as mentioned previously, corresponds to a purely synchronous steady-state response.

With the autobalancer present, the simulation results in Fig. 20 show that after the first blade is lost, the autobalancer balls do not settle down to a fixed point. Rather, the balancer balls continue to oscillate in a stable limit cycle about the balanced condition (see Fig. 20c). As a result, the net autobalancer force is not synchronous with the bladed disk. Even so, in this case, as evidenced by comparing bearing-load responses in Figs. 19a and 20a, the time-averaged nonsynchronous autobalancer force effectively acts to reduce the bearing load compared with the no-autobalancer case. Furthermore, the blade-tip deflections are also reduced (see Figs. 19b and 20b). However, due to the system nonlinearity, the benefits of the autobalancer in the unstable operating-speed regions cannot be guaranteed, since the nonsynchronous limit-cycle amplitude is a function of initial conditions.

Along these lines, the balancer-ball initial positions can strongly affect the global reachability of the fixed-point equilibrium configurations [9,10]. Thus, even when the fixed-point equilibrium analysis predicts a stable balanced condition, this is not an indication about the global stability, since other stable limit cycles may coexist that do not produce the desired balancing effect. However, consistent with results of previous investigations for rigid-rotor/autobalancer systems [9,10], the time-domain simulation results for the bladed-disk/autobalancer system presented in this study found that balancer-ball initial positions satisfying $\phi_{b2}(0) = \phi_{b1}(0) + \pi$, lie within the basin of attraction of the balanced equilibrium. The blade-loss simulation results also validate the stability and steady-state response analysis method developed in Secs. III and IV for bladed-disk/autobalancer systems.

VI. Conclusions

This paper conducts a pioneering study into the use of a passive automatic-balancing device for balancing a bladed-disk system under blade-loss conditions. Here, a dynamic model of a bladed-disk/shaft/bearing system equipped with a passive dual-ball automatic-balancing device is developed, including lateral bearing flexiblity, in-plane blade flexibility, and shaft torsional dynamics. The model also includes the effects of blade aerodynamic drag and imbalance for a general asymmetric blade pattern. An asymmetric blade pattern (e.g., due to a lost blade) results in a net synchronous mass and aerodynamic imbalance acing on the hub. A stability and a steady-state response analysis of the nonlinear bladed-disk/autobalancer system is developed to explore the autobalancer effectiveness in counteracting the synchronous imbalance resulting from a missing blade.

Similar to previous automatic-balancing studies on simple rotors, it is discovered that there exist three types of fixed-point balancer-ball equilibrium configurations for the bladed-disk/autobalancer system. Specifically, these are referred to as the merged, opposed, and balanced configurations. However, their solution process is more involved than with simple rotors, due to dynamic coupling between the balancer balls and the in-plane blade motions. In the balanced condition, the hub lateral deflections (and bearing load) is suppressed to zero. The analysis shows that by properly sizing the autobalancer and with sufficient ball/track damping, this desired balanced condition is naturally achieved and is stable at supercritical speeds above the bladed-disk first lateral-mode crossing speed. This is generally true with the exception of two types of unstable speed ranges that must be avoided. One type of instability is a rotordynamic instability that arises from torsion/lateral coupling induced by blade-pattern asymmetry from the missing blade. The second instability is due to the automatic balancer and occurs at speeds just above the bladed-disk first lateral-mode crossing speed. At supercritical speeds outside the unstable speed ranges, the autobalancer reaches the balanced equilibrium and reduces both the lateral bearing load and blade-tip deflections.

In addition to producing a synchronous aerodynamic imbalance that is 90° out of phase with the blade mass imbalance, the blade aerodynamic drag coefficient has destabilizing effects on automatic-balancing behavior. This is illustrated by the fact that the amount of ball-track damping required for stable automatic balancing increases for larger values of blade drag coefficient. Furthermore, since the bladed-disk aerodynamic imbalance contains terms that are proportional to both Ω^2 and Ω^4, an autobalancer that is sized to cancel imbalance at a lower design speed may saturate at higher speeds. This does not occur for the case of a pure mass imbalance and thus constitutes a fundamentally new result with important implications on the sizing of autobalancers for bladed-disk applications.

In addition to the steady-state response and stability analysis, the transient response to a blade-loss scenario is investigated via numerical time-domain integration of the full nonlinear bladed-disk/autobalancer system equations. The simulation results for a multiple-blade-loss scenario numerically confirm the steady-state and stability analysis predictions. When the system is simulated at a supercritical operating speed outside the predicted instability zones, the autobalancer successfully self-adjusts to counteract the mass and aerodynamic imbalance resulting from a sudden blade loss. In addition to suppressing the steady-state response, the autobalancer also tends to reduce the peak transient bearing load and blade defections during the blade-loss event. Furthermore, when the system is simulated at an operating speed just above the first critical speed at which the analysis predicts that no stable automatic-balancing solution exists, the results show that the autobalancer balls execute a nonsynchronous limit cycle that oscillates about the balanced condition.

The new analysis methods and results from this investigation demonstrate that automatic balancing of bladed disks could be an attractive option for reducing the severity of blade-loss events in turbomachinery applications. The results of this analysis warrant future studies to include a more detailed unsteady aerodynamic model and the effects of out-of-plane flexibility.

Appendix

The bladed-disk subsystem matrices and mass-imbalance force terms in Eq. (12) are given in Eqs. (A1–A4):

$$\mathbf{M}_{\text{blisk}} = \begin{bmatrix} m_{\text{blisk}} & 0 & -I_s & -m_1 \sin\psi_1 \mathbf{D}_1 & \cdots & -m_{N_b} \sin\psi_{N_b} \mathbf{D}_{N_b} \\ 0 & m_{\text{blisk}} & I_c & m_1 \cos\psi_1 \mathbf{D}_1 & \cdots & m_{N_b} \cos\psi_{N_b} \mathbf{D}_{N_b} \\ -I_s & I_c & J_{\text{blisk}} & m_1 \mathbf{F}_1 & \cdots & m_{N_b} \mathbf{F}_{N_b} \\ -m_1 \sin\psi_1 \mathbf{D}_1^T & m_1 \cos\psi_1 \mathbf{D}_1^T & m_1 \mathbf{F}_1^T & m_1 \mathbf{A}_1 & 0 & 0 \\ \vdots & \vdots & \vdots & 0 & \ddots & 0 \\ -m_{N_b} \sin\psi_{N_b} \mathbf{D}_{N_b}^T & m_{N_b} \cos\psi_{N_b} \mathbf{D}_{N_b}^T & m_{N_b} \mathbf{F}_{N_b}^T & 0 & 0 & m_{N_b} \mathbf{A}_{N_b} \end{bmatrix} \tag{A1}$$

$$\mathbf{C}_{\text{blisk}} = \begin{bmatrix} c_s & -2\Omega m_{\text{blisk}} & -2\Omega I_c & -2\Omega m_1 \cos\psi_1 \mathbf{D}_1 & \cdots & -2\Omega m_{Nb} \cos\psi_{N_b} \mathbf{D}_{N_b} \\ 2\Omega m_{\text{blisk}} & c_s & -2\Omega I_s & -2\Omega m_1 \sin\psi_1 \mathbf{D}_1 & \cdots & -2\Omega m_{Nb} \sin\psi_{N_b} \mathbf{D}_{N_b} \\ 2\Omega I_c & 2\Omega I_s & c_t & \mathbf{0}_{1\times N_m} & \cdots & \mathbf{0}_{1\times N_m} \\ 2\Omega m_1 \cos\psi_1 \mathbf{D}_1^T & 2\Omega m_1 \sin\psi_1 \mathbf{D}_1^T & \mathbf{0}_{N_m\times 1} & \xi EI_1 \mathbf{B}_1 & 0 & 0 \\ \vdots & \vdots & \vdots & 0 & \ddots & 0 \\ 2\Omega m_{N_b} \cos\psi_{N_b} \mathbf{D}_{N_b}^T & 2\Omega m_{N_b} \sin\psi_{N_b} \mathbf{D}_{N_b}^T & \mathbf{0}_{N_m\times 1} & 0 & 0 & \xi EI_{N_b} \mathbf{B}_{N_b} \end{bmatrix} \tag{A2}$$

$$\mathbf{K}_{\text{blisk}} = \begin{bmatrix} k_s - m_{\text{blisk}}\Omega^2 & -c_s\Omega & 0 & m_1\Omega^2 \sin\psi_1 \mathbf{D}_1 & \cdots & m_{N_b}\Omega^2 \sin\psi_{N_b} \mathbf{D}_{N_b} \\ c_s\Omega & k_s - m_{\text{blisk}}\Omega^2 & 0 & -m_1\Omega^2 \cos\psi_1 \mathbf{D}_1 & \cdots & -m_{N_b}\Omega^2 \cos\psi_{N_b} \mathbf{D}_{N_b} \\ 0 & 0 & k_t & \mathbf{0}_{1\times N_m} & \cdots & \mathbf{0}_{1\times N_m} \\ m_1\Omega^2 \sin\psi_1 \mathbf{D}_1^T & -m_1\Omega^2 \cos\psi_1 \mathbf{D}_1^T & \mathbf{0}_{N_m\times 1} & EI_1 \mathbf{B}_1 + m_1\Omega^2(\mathbf{C}_1 - \mathbf{A}_1) & 0 & 0 \\ \vdots & \vdots & \vdots & 0 & \ddots & 0 \\ m_{N_b}\Omega^2 \sin\psi_{N_b} \mathbf{D}_{N_b}^T & -m_{N_b}\Omega^2 \cos\psi_{N_b} \mathbf{D}_{N_b}^T & \mathbf{0}_{N_m\times 1} & 0 & 0 & EI_{N_b} \mathbf{B}_{N_b} + m_{N_b}\Omega^2(\mathbf{C}_{N_b} - \mathbf{A}_{N_b}) \end{bmatrix} \tag{A3}$$

$$\mathbf{F}_{\text{imb}} = \Omega^2 \begin{bmatrix} \sum_{i=1}^{N_b} m_i L_i (\frac{L_i}{2} + R_h) \cos\psi_i \\ \sum_{i=1}^{N_b} m_i L_i (\frac{L_i}{2} + R_h) \sin\psi_i \\ 0 \\ \mathbf{0}_{N_m\times 1} \\ \vdots \\ \mathbf{0}_{N_m\times 1} \end{bmatrix} \tag{A4}$$

with

$$\mathbf{A}_i = \int_0^{L_i} \Phi_i(x)^T \Phi_i(x)\, \mathrm{d}x, \qquad \mathbf{B}_i = \int_0^{L_i} \Phi_i''(x)^T \Phi_i''(x)\, \mathrm{d}x, \qquad \mathbf{C}_i = \int_0^{L_i} \left[(R_h + x) \int_0^x \Phi_i'(\chi)^T \Phi_i'(\chi)\, \mathrm{d}\chi \right] \mathrm{d}x$$
$$\mathbf{D}_i = \int_0^{L_i} \Phi_i(x)\, \mathrm{d}x, \qquad \mathbf{F}_i = \int_0^{L_i} (R_h + x) \Phi_i(x)\, \mathrm{d}x \qquad \mathbf{G}_i = \int_0^{L_i} (R_h + x)^2 \Phi_i(x)\, \mathrm{d}x, \qquad \mathbf{H}_i = \int_0^{L_i} (R_h + x) \Phi_i(x)^T \Phi_i(x)\, \mathrm{d}x \tag{A5}$$

and

$$m_{\text{blisk}} = m_h + \sum_{i=1}^{N_b} m_i L_i, \qquad J_{\text{blisk}} = J_{\text{hub}} + \sum_{i=1}^{N_b} \left[\frac{m_i L_i^3}{12} + m_i L_i \left(R_h + \frac{L_i}{2} \right)^2 \right] \tag{A6}$$

$$I_c = \sum_{i=1}^{N_b} \left[m_i L_i \left(\frac{L_i}{2} + R_h \right) \cos\psi_i \right], \qquad I_s = \sum_{i=1}^{N_b} \left[m_i L_i \left(\frac{L_i}{2} + R_h \right) \sin\psi_i \right] \tag{A7}$$

and with blade deflections expanded as

$$w_i(x_i, t) = \sum_{j=1}^{N_m} \varphi_{ij}(x) \eta_{ij}(t) = \Phi_i(x) \boldsymbol{\eta}_i(t) \tag{A8}$$

where $\Phi_i(x)$ is the $1 \times N_m$ shape function vector of the ith blade. Furthermore, the aerodynamic damping, stiffness, and forcing terms in Eq. (12) are given by Eqs. (A9–A11):

$$\mathbf{C}_{\text{aero}} = 2\Omega c_d \begin{bmatrix} \frac{1}{2}\sum_{i=1}^{N_b}[(L_i+R_h)^2-R_h^2]\sin^2\psi_i & -\frac{1}{2}\sum_{i=1}^{N_b}[(L_i+R_h)^2-R_h^2]\cos\psi_i\sin\psi_i & & & \\ -\frac{1}{2}\sum_{i=1}^{N_b}[(L_i+R_h)^2-R_h^2]\cos\psi_i\sin\psi_i & \frac{1}{2}\sum_{i=1}^{N_b}[(L_i+R_h)^2-R_h^2]\cos^2\psi_i & \text{sym} & & \\ -\frac{1}{3}\sum_{i=1}^{N_b}[(L_i+R_h)^3-R_h^3]\sin\psi_i & \frac{1}{3}\sum_{i=1}^{N_b}[(L_i+R_h)^3-R_h^3]\cos\psi_i & \frac{1}{4}\sum_{i=1}^{N_b}[(L_i+R_h)^4-R_h^4] & & \\ -\sin\psi_1\mathbf{F}_1^T & \cos\psi_1\mathbf{F}_1^T & \mathbf{G}_1^T & \mathbf{H}_1 & \\ \vdots & \vdots & \vdots & 0 & \ddots \\ -\sin\psi_{N_b}\mathbf{F}_{N_b}^T & \cos\psi_{N_b}\mathbf{F}_{N_b}^T & \mathbf{G}_{Nb}^T & 0 & 0 \quad \mathbf{H}_{N_b} \end{bmatrix} \tag{A9}$$

$$\mathbf{K}_{\text{aero}} = 2c_d\Omega^2 \begin{bmatrix} -\frac{1}{2}\sum_{i=1}^{N_b}[(L_i+R_h)^2-R_h^2]\cos\psi_i\sin\psi_i & -\frac{1}{2}\sum_{i=1}^{N_b}[(L_i+R_h)^2-R_h^2]\sin^2\psi_i & 0 & \mathbf{0}_{1\times N_m} & \cdots & \mathbf{0}_{1\times N_m} \\ \frac{1}{2}\sum_{i=1}^{N_b}[(L_i+R_h)^2-R_h^2]\cos^2\psi_i & \frac{1}{2}\sum_{i=1}^{N_b}[(L_i+R_h)^2-R_h^2]\cos\psi_i\sin\psi_i & 0 & \mathbf{0}_{1\times N_m} & \cdots & \mathbf{0}_{1\times N_m} \\ \frac{1}{3}\sum_{i=1}^{N_b}[(L_i+R_h)^3-R_h^3]\cos\psi_i & \frac{1}{3}\sum_{i=1}^{N_b}[(L_i+R_h)^3-R_h^3]\sin\psi_i & 0 & \mathbf{0}_{1\times N_m} & \cdots & \mathbf{0}_{1\times N_m} \\ \cos\psi_1\mathbf{F}_1^T & \sin\psi_1\mathbf{F}_1^T & \mathbf{0}_{N_m\times 1} & \mathbf{0}_{N_m\times N_m} & \cdots & \mathbf{0}_{N_m\times N_m} \\ \vdots & \vdots & \vdots & \vdots & \ddots & \vdots \\ \cos\psi_{N_b}\mathbf{F}_{N_b}^T & \sin\psi_{N_b}\mathbf{F}_{N_b}^T & \mathbf{0}_{N_m\times 1} & \mathbf{0}_{N_m\times N_m} & \cdots & \mathbf{0}_{N_m\times N_m} \end{bmatrix} \tag{A10}$$

$$\mathbf{F}_{\text{aero}} = c_d\Omega^2 \begin{bmatrix} \frac{1}{3}\sum_{i=1}^{N_b}[(L_i+R_h)^3-R_h^3]\sin\psi_i \\ -\frac{1}{3}\sum_{i=1}^{N_b}[(L_i+R_h)^3-R_h^3]\cos\psi_i \\ -\frac{1}{4}\sum_{i=1}^{N_b}[(L_i+R_h)^4-R_h^4] \\ -\mathbf{G}_1^T \\ \vdots \\ -\mathbf{G}_{N_b}^T \end{bmatrix} \tag{A11}$$

The autobalancer subsystem matrices and force terms in Eq. (12) are given in Eqs. (A12–A15):

$$\mathbf{M}_{\text{AB}} = \begin{bmatrix} 2m_b & 0 & -m_bR_b(\sin\phi_{b_1}+\sin\phi_{b_2}) & \cdots \\ 0 & 2m_b & m_bR_b(\cos\phi_{b_1}+\cos\phi_{b_2}) & \\ -m_bR_b(\sin\phi_{b_1}+\sin\phi_{b_2}) & m_bR_b(\cos\phi_{b_1}+\cos\phi_{b_2}) & 2m_bR_b^2 & \\ -m_bR_b\sin\phi_{b_1} & m_bR_b\cos\phi_{b_1} & m_bR_b^2 & \\ -m_bR_b\sin\phi_{b_2} & m_bR_b\cos\phi_{b_2} & m_bR_b^2 & \end{bmatrix}$$

$$\begin{bmatrix} -m_bR_b\sin\phi_{b_1} & -m_bR_b\sin\phi_{b_2} \\ m_bR_b\cos\phi_{b_1} & m_bR_b\cos\phi_{b_2} \\ \cdots \quad m_bR_b(R_b+v_h\cos\phi_{b_1}+w_h\sin\phi_{b_1}) & m_bR_b(R_b+v_h\cos\phi_{b_2}+w_h\sin\phi_{b2}) \\ m_bR_b^2 & 0 \\ 0 & m_bR_b^2 \end{bmatrix} \tag{A12}$$

$$\mathbf{C}_{\text{AB}} = \begin{bmatrix} 0 & -4m_b\Omega & -2m_bR_b((\Omega+\dot{\phi}_{b_1})\cos\phi_{b_1}+(\Omega+\dot{\phi}_{b_2})\cos\phi_{b_2}) & \cdots \\ 4m_b\Omega & 0 & -2m_bR_b((\Omega+\dot{\phi}_{b_1})\sin\phi_{b_1}+(\Omega+\dot{\phi}_{b_2})\sin\phi_{b_2}) & \\ 2m_bR_b\Omega(\cos\phi_{b_1}+\cos\phi_{b_2}) & 2m_bR_b\Omega(\sin\phi_{b_1}+\sin\phi_{b_2}) & 0 & \\ 2m_bR_b\Omega\cos\phi_{b_1} & 2m_bR_b\Omega\sin\phi_{b_1} & 0 & \\ 2m_bR_b\Omega\cos\phi_{b_2} & 2m_bR_b\Omega\sin\phi_{b_1} & 0 & \end{bmatrix}$$

$$\begin{bmatrix} -2m_bR_b\Omega\cos\phi_{b_1} & -2m_bR_b\Omega\cos\phi_{b_2} \\ -2m_bR_b\Omega\sin\phi_{b_1} & -2m_bR_b\Omega\sin\phi_{b_2} \\ \cdots \quad -m_bR_b(2\Omega+\dot{\phi}_{b_1})(v_h\sin\phi_{b_1}-w_h\cos\phi_{b_1}) & -m_bR_b(2\Omega+\dot{\phi}_{b_2})(v_h\sin\phi_{b_2}-w_h\cos\phi_{b_2}) \\ c_bR_b^2 & 0 \\ 0 & c_bR_b^2 \end{bmatrix} \tag{A13}$$

$$\mathbf{K}_{\text{AB}} = m_b\Omega^2 \begin{bmatrix} -2 & 0 & 0 & 0 & 0 \\ 0 & -2 & 0 & 0 & 0 \\ 0 & 0 & 0 & 0 & 0 \\ R_b\sin\phi_{b_1} & -R_b\cos\phi_{b_1} & 0 & 0 & 0 \\ R_b\sin\phi_{b_2} & -R_b\cos\phi_{b_2} & 0 & 0 & 0 \end{bmatrix} \tag{A14}$$

$$\mathbf{F}_{\mathrm{AB}} = m_b R_b \begin{bmatrix} (\Omega^2 + \dot{\phi}_{b_1}^2)\cos\phi_{b_1} + (\Omega^2 + \dot{\phi}_{b_2}^2)\cos\phi_{b_2} \\ (\Omega^2 + \dot{\phi}_{b_1}^2)\sin\phi_{b_1} + (\Omega^2 + \dot{\phi}_{b_2}^2)\sin\phi_{b_2} \\ 0 \\ 0 \\ 0 \end{bmatrix} \tag{A15}$$

Acknowledgments

This research was supported by the National Science Foundation under grant number NSF-CMMI-0856471. The author would also like to acknowledge the proofreading efforts of Daeyi Jung.

References

[1] Thearle, E. L., "Automatic Dynamic Balancers, Part 2: Ring, Pendulum, Ball Balancers," *Machine Design*, Vol. 22, Oct. 1950, pp. 103–106.

[2] Bovik, P., and Hogfords, C., "Autobalancing of Rotors," *Journal of Sound and Vibration*, Vol. 111, No. 3, 1986, pp. 429–440. doi:10.1016/S0022-460X(86)81402-X

[3] Majewski, T., "Position Errors Occurrence in Self Balancers Used on Rigid Rotors of Rotating Machinery," *Mechanism and Machine Theory*, Vol. 23, No. 1, 1988, pp. 71–78. doi:10.1016/0094-114X(88)90011-0

[4] Jinnouchi, Y., Araki, Y., Inoue, J., Ohtsuka, Y., and Tan, C., "Automatic Balancer (Static Balancing and Transient Response of a Multi-Ball Balancer)," *Transactions of the Japan Society of Mechanical Engineers. Series C*, Vol. 59, No. 557, Jan. 1993, pp. 79–84.

[5] Lindell, H., "Vibration Reduction on Hand-Held Grinders by Automatic Balancers," *Central European Journal of Public Health*, Vol. 4, No. 1, Feb. 1996, pp. 43–45.

[6] Rajalingham, C., and Rakheja, S., "Whirl Suppression in Hand-Held Power Tool Rotors Using Guided Rolling Balancers," *Journal of Sound and Vibration*, Vol. 217, No. 3, 1998, pp. 453–466. doi:10.1006/jsvi.1998.1780

[7] Rajalingham, C., Bhat, R. B., and Rakheja, S., "Automatic Balancing of Flexible Vertical Rotors Using a Guided Ball," *International Journal of Mechanical Sciences*, Vol. 40, No. 9, 1998, pp. 825–834. doi:10.1016/S0020-7403(98)80004-0

[8] Chung, J., and Ro, D. S., "Dynamic Analysis of an Automatic Dynamic Balancer for Rotating Mechanisms," *Journal of Sound and Vibration*, Vol. 228, No. 5, 1999, pp. 1035–1056. doi:10.1006/jsvi.1999.2456

[9] Green, K., Champneys, A. R., and Lieven, N. J., "Bifurcation Analysis of an Automatic Dynamic Balancing Mechanism for Eccentric Rotors," *Journal of Sound and Vibration*, Vol. 291, Nos. 3–5, 2006, pp. 861–881. doi:10.1016/j.jsv.2005.06.042

[10] Green, K., Champneys, A. R., and Friswell, M. I., "Analysis of the Transient Response of an Automatic Balancer for Eccentric Rotors," *International Journal of Mechanical Sciences*, Vol. 48, No. 3, 2006, pp. 274–293. doi:10.1016/j.ijmecsci.2005.09.014

[11] Chung, J., and Jang, I., "Dynamic Response and Stability Analysis of an Automatic Ball Balancer for a Flexible Rotor," *Journal of Sound and Vibration*, Vol. 259, No. 1, 2003, pp. 31–43. doi:10.1006/jsvi.2002.5137

[12] Rajalingham, C., and Bhat, R. B., "Complete Balancing of a Disk Mounted on a Vertical Cantilever Shaft Using a Two Ball Automatic Balancer," *Journal of Sound and Vibration*, Vol. 290, Nos. 1–2, Feb. 2006, pp. 161–191. doi:10.1016/j.jsv.2005.03.025

[13] Chao, P. C. P., Huang, Y. D., and Sung, C. K., "Non-planar Dynamic Modeling for the Optical Disk Drive Spindles Equipped with and Automatic Balancer," *Mechanism and Machine Theory*, Vol. 38, No. 11, 2003, pp. 1289–1305. doi:10.1016/S0094-114X(03)00078-8

[14] Chao, P. C. P., Sung, C. K., Wu, S. T., and Huang, J. S., "Non-Planar Modeling and Experimental Validation of a Spindle-Disk System Equipped with an Automatic Balancer System in Optical Disk Drives," *Microsystem Technologies*, Vol. 13, Nos. 8–10, 2007, pp. 1227–1239. doi:10.1007/s00542-006-0337-2

[15] Kim, W., Lee, D. J., and Chung, J., "Three-Dimensional Modelling and Dynamic Analysis of an Automatic Ball Balancer in an Optical Disk Drive," *Journal of Sound and Vibration*, Vol. 285, No. 3, 2005, pp. 547–569. doi:10.1016/j.jsv.2004.08.016

[16] DeSmidt, H. A., "Imbalance Vibration Suppression of Supercritical Shafts with Automatic Balancing Devices," *Proceedings of the ASME Design Engineering Technical Conference-21st Biennial Conference on Mechanical Vibration and Noise*, ASME International, New York, Sept. 2007.

[17] Ehyaei, J., and Moghaddam, M. M., "Dynamic Response and Stability Analysis of an Unbalanced Flexible Rotating Shaft Equipped with N Automatic Ball-Balancers," *Journal of Sound and Vibration*, Vol. 321, Nos. 3–5, 2009, pp. 554–571. doi:10.1016/j.jsv.2008.10.019

[18] Sohn, J. S., Lee, J. W., Cho, E. H., Park, N. C., and Park, Y. P., "Dynamic Analysis of a Pendulum Dynamic Automatic Balancer," *Shock and Vibration*, Vol. 14, No. 2, 2007, pp. 151–167.

[19] Horvath, R., Flowers, G. T., and Fausz, J., "Passive Balancing of Rotor Systems Using Pendulum Balancers," *Journal of Vibration and Acoustics*, Vol. 130, No. 4, 2008, Paper 041011. doi:10.1115/1.2731401

[20] Lee, J., and Moorham, W. K. V., "Analytical and Experimental Analysis of a Self-Compensating Dynamic Balancer in a Rotating Mechanism," *Journal of Dynamic Systems, Measurement, and Control*, Vol. 118, No. 3, 1996, pp. 468–475. doi:10.1115/1.2801169

[21] Lu, C. J., Wang, M. C., and Huang, S. H., "Analytical Study of the Stability of a Two-Ball Automatic Balancer," *Mechanical Systems and Signal Processing*, Vol. 23, No. 3, 2009, pp. 884–896. doi:10.1016/j.ymssp.2008.06.008

[22] Hodges, D. H., and Pierce, G. A., *Introduction to Structural Dynamics and Aeroelasticity*, Cambridge Univ. Press, New York, 2002.

[23] Meirovitch, L., *Analytical Methods in Vibrations*, Macmillan, New York, 1967.

[24] Bucher, I., and Ewins, D. J., "Modal Analysis and Testing of Rotating Structures," *Philosophical Transactions of the Royal Society of London, Series A: Mathematical, Physical, and Engineering Sciences*, Vol. 359, No. 1778, Jan. 2001, pp. 61–96. doi:10.1098/rsta.2000.0714

J. Wei
Associate Editor